Title

Quaternary structure independent folding of voltage-gated ion channel pore domain subunits

Journal

Nature Structural & Molecular Biology, 29(6)

ISSN

1545-9993

Authors

Arrigoni, Cristina
Lolicato, Marco
Shaya, David
et al.

Publication Date

2022-06-01

DOI

10.1038/s41594-022-00775-x

Published in final edited form as:

Nat Struct Mol Biol. 2022 June ; 29(6): 537–548. doi:10.1038/s41594-022-00775-x.

Quaternary structure independent folding of voltage-gated ion channel pore domain subunits

Cristina Arrigoni[1,9], **Marco Lolicato**[1,9], **David Shaya**[1], **Ahmed Rohaim**[1], **Felix Findeisen**[1], **Lam-Kiu Fong**[1,2], **Claire M. Colleran**[1], **Pawel Dominik**[3], **Sangwoo S. Kim**[3], **Jonathan P. Schuermann**[4], **William F. DeGrado**[1,2], **Michael Grabe**[1,2], **Anthony A. Kossiakoff**[3], **Daniel L. Minor Jr.**[1,5,6,7,8]

[1]Cardiovascular Research Institute, University of California, San Francisco, CA, USA.

[2]Department of Pharmaceutical Chemistry, University of California, San Francisco, CA, USA.

[3]Department of Biochemistry and Molecular Biology, University of Chicago, Chicago, IL, USA.

[4]Northeastern Collaborative Access Team, Department of Chemistry and Chemical Biology, Cornell University, Ithaca, NY, USA.

[5]Departments of Biochemistry and Biophysics, and Cellular and Molecular Pharmacology, University of California, San Francisco, CA, USA.

[6]California Institute for Quantitative Biomedical Research, University of California, San Francisco, CA, USA.

[7]Kavli Institute for Fundamental Neuroscience, University of California, San Francisco, CA, USA.

Correspondence and requests for materials should be addressed to Daniel L. Minor. daniel.minor@ucsf.edu.

Author contributions

C. A. and D. L. M. conceived the study and designed the experiments. D. S. purified and crystallized the initial structures of Ca_VSp1p and Na_VAb1p in detergent. A. R. purified, crystallized, and determined the structure of Na_VAb1p in bicelles. M. L. determined the structures of the $Na_V Ae1_{Sp1CTD}$p and the SAT09 and ANT05 complexes, and refined all of the structures. F. F. determined structures of Ca_VSp1p and Na_VAb1p in detergent. C. M. C. and C. A. expressed and purified the proteins and sFab complexes. C. A. crystallized $Na_V Ae1/Sp1_{CTD}$p and the SAT09 and ANT05 complexes and performed the biochemical characterization. P. D. and A. A. K. provided the platform for the development of sFabs. P. D. and S. S. K. selected the sFabs. J. P. S. contributed to the ANT05 complex data collection and structure determination. L.-K. F. performed the simulations. L.-K. F., W. F. D. and M. G. analyzed the simulations. D. L. M. analyzed data and provided guidance and support. C. A., M. L., L.-K. F., W. F. D., M. G. and D. L. M. wrote the paper.

online content

Any methods, additional references, Nature Research reporting summaries, source data, extended data, supplementary information, acknowledgements, peer review information; details of author contributions and competing interests; and statements of data and code availability are available at https://doi.org/10.1038/s41594–022-00775-x.

Competing interests

The other authors declare no competing interests.

Extended data is available for this paper at https://doi.org/10.1038/s41594-022-00775-x.

Supplementary information The online version contains supplementary material available at https://doi.org/10.1038/s41594-022-00775-x.

Peer review information Nature Structural and Molecular Biology thanks the anonymous reviewers for their contribution to the peer review of this work.

Editor recognition statement Primary Handling editor: Florian Ullrich, in collaboration with the Nature Structural & Molecular Biology team. Peer reviewer reports are available.

[8]Molecular Biophysics and Integrated Bio-imaging Division, Lawrence Berkeley National Laboratory, Berkeley, CA, USA.

[9]Present address: Department of Molecular Medicine, University of Pavia, Pavia, Italy.

Abstract

Every voltage-gated ion channel (VGIC) has a pore domain (PD) made from four subunits, each comprising an antiparallel transmembrane helix pair bridged by a loop. The extent to which PD subunit structure requires quaternary interactions is unclear. Here, we present crystal structures of a set of bacterial voltage-gated sodium channel ($BacNa_V$) 'pore only' proteins that reveal a surprising collection of non-canonical quaternary arrangements in which the PD tertiary structure is maintained. This context-independent structural robustness, supported by molecular dynamics simulations, indicates that VGIC-PD tertiary structure is independent of quaternary interactions. This fold occurs throughout the VGIC superfamily and in diverse transmembrane and soluble proteins. Strikingly, characterization of PD subunit-binding Fabs indicates that non-canonical quaternary PD conformations can occur in full-length VGICs. Together, our data demonstrate that the VGIC-PD is an autonomously folded unit. This property has implications for VGIC biogenesis, understanding functional states, de novo channel design, and VGIC structural origins.

The VGIC superfamily is the largest channel family[1]. VGIC transmembrane architecture is built from two elements. Each subunit contains a PD comprising two transmembrane helices bridged by the pore helix and selectivity filter (SF)[2]. Some superfamily members also have a four-transmembrane-helix voltage-sensor or voltage-sensor-like domain (VSD)[3–5]. Regardless of whether a VGIC assembles from multiple chains (for example potassium[2,6] and TRP channels[3]) or carries all subunits in one polypeptide (for example voltage-gated calcium (Ca_Vs) and sodium channels (Na_Vs)[4]), the ion-conductive pore comes into being only upon assembly of four PD subunits[2–6].

There is a growing appreciation that VGIC subunits are modular. VSDs can adopt a native-like structure independent from the PD[7–9], and protein dissection studies, particularly of bacterial sodium channels ($BacNa_V$s)[10–14], have established PD structural independence. Such 'pore only' proteins lacking the VSD can form selective ion channels[10–13,15,16] and maintain the canonical VGIC quaternary pore structure[11,12,17–20]. Nevertheless, how four PD subunits assemble into a functional pore and whether there are stable intermediates remains poorly understood[21,22]. Labeling studies of $K_V1.3$ (refs. [23,24]) and archaeal KvAP[25] channels have suggested that a native-like pore helix topology can develop within a single PD subunit, independent of tetramer formation. However, sub-microsecond (~650 ns) molecular dynamics (MD) simulations indicate that the PD tertiary fold is stable[23], and a VGIC-PD has never been observed in any form except for the native tetrameric assembly.

Here, we present multiple $BacNa_V$s pore-only structures together with tens of microseconds of MD simulations that demonstrate that the PD tertiary architecture, the VGIC-PD fold, forms independently of quaternary structure details. Structural comparisons find the VGIC-PD fold throughout the VGIC superfamily, in other channels and transporters, and in transmembrane and soluble proteins that are not channels. The shared features suggest that the VGIC-PD fold is built from an ancient scaffold comprising an antiparallel helical

pair bridged by a loop. The capacity of such a structure to fold independently agrees with long-standing ideas of membrane-protein-folding mechanisms[26,27] and cysteine accessibility studies suggesting that Kv PDs adopt native-like topologies during folding[23–25]. The structural independence of the VGIC-PD fold has implications for VGIC biogenesis and understanding disease mutant effects, may have a role in functional states, and provides clues about possible structural origins of the VGIC pore.

Results

BacNa$_V$ ‘pore only’ structures show non-canonical assemblies.

We determined crystal structures of three pore-only BacNa$_V$s: *Alcanivorax borkumensis* Na$_V$Ab1p[10], a *Silicibacter pomeroyi* Na$_V$Sp1 calcium-selective mutant, Ca$_V$Sp1p[10], and a chimera with the *Alkalilimnicola ehrlichii* Na$_V$Ae1 PD[18,28] and Na$_V$Sp1 carboxy-terminal domain (CTD), Na$_V$Ae1/Sp1$_{CTD}$p, at resolutions of 2.85 Å, 3.5 Å, and 4.19 Å, respectively (Table 1 and Table 2). All formed tetramers composed of PD monomers with the canonical tertiary fold encompassing the S5 and S6 transmembrane helices bridged by the P1 and P2 helices and SF[14] (Fig. 1a). To our surprise, the PD subunits in each were arranged in non-canonical quaternary assemblies in which the SF faced the periphery rather than the central axis (Fig. 1b–d).

The Na$_V$Ab1p structure, inside-out$_A$, showed the most extreme deviation from the canonical quaternary structure (Fig. 1b and Extended Data Fig. 1a–d) and was observed in crystals grown from detergent and lipid bicelles that diffracted to 2.85 Å and 3.64 Å, respectively (Table 1). The two structures were very similar (root-mean-square deviation, RMSD$_{C\alpha}$ = 0.613 and 0.733 for detergent Na$_V$Ab1p to bicelle Na$_V$Ab1p tetramers A and B, respectively) (Extended Data Fig. 1e). This similarity, together with the presence of a lipid in the 2.85-Å detergent structure next to a P1 helix aromatic residue where a similar lipid is found in the canonical pore conformation (Extended Data Fig. 1f), indicates that the unusual quaternary arrangement was not a consequence of the absence of lipids.

In inside-out$_A$, each PD monomer is rotated ~180° around the channel central axis relative to the canonical pore structure typified by Na$_V$Ae1p[11,18] (Fig. 1b,e). This places the S5 transmembrane helices along the central fourfold axis where they make extensive interactions with each other while the S6 helices face the periphery. These changes result in increased buried surface area of the individual PDs by ~281 Å^2 relative to the canonical arrangement found in Na$_V$Ae1p[11,18] (Supplementary Table 1). The neck domain is composed of largely hydrophilic residues and forms a continuous helix that connects the C-terminal end of S6 with the amino-terminal end of the coiled-coil (Fig. 1b and Extended Data Fig. 1d). Despite the dramatic PD quaternary structure rearrangement, the Na$_V$Ab1p coiled-coil domain matches other BacNa$_V$ structures[11,18] having the coiled-coil sequence ‘a’ and ‘d’ hydrophobic residues[18,29] in its interior and hydrophilic residues on its exterior (Fig. 1b).

Ca$_V$Sp1p and Na$_V$Ae1/Sp1$_{CTD}$p also showed non-canonical quaternary arrangements. Ca$_V$Sp1p crystals were grown from seleno-methionine-labeled protein reconstituted in lipid bicelles, diffracted at 3.5 Å, and were solved by a two-wavelength MAD experiment (Table

1). In the Ca_VSp1p quaternary structure, S5 is on the periphery, and S6 lines the tetramer central axis, similar to canonical PDs[11,18] (Fig. 1c,e and Extended Data Fig. 1g,i). However, each PD subunit has undergone a ~45° clockwise rotation relative to the central axis. This allows the S6 helices to contact each other in a way that closes the central cavity and places the SF along the bilayer facing the structure periphery, termed $peripheral_{SF}$ (Fig. 1c). The $peripheral_{SF}$ arrangement has more surface area per monomer buried (~123 $Å^2$) than does the canonical structure (Supplementary Table 1). There is a kink at Ala226 where the S6 C-terminal end joins the continuous helix comprising the neck and coiled-coil domains (Extended Data Fig. 1k). The Ca_VSp1p coiled-coil 'a–d' hydrophobic repeat forms the interior of the four-helix bundle, as in CTDs of the canonical Na_VAe1p[11,18] (Fig. 1c) and inside-out Na_VAb1p (Fig. 1b). Hence, as with Na_VAb1p, the principal quaternary rearrangement from the canonical structure occurs in the Ca_VSp1p PD.

$Na_VAe1/Sp1_{CTD}p$ crystals that diffracted to 4.19 Å were solved by MAD using the anomalous signal from seleno-methionine-containing crystals (Table 1) and had two tetramers in the asymmetric unit. Each showed variations on the $inside\text{-}out_A$ form, termed $inside\text{-}out_B$ and $inside\text{-}out_C$ (Fig. 1d and Extended Data Fig. 1l–q). As with $inside\text{-}out_A$, S5 lines the central axis of both $inside\text{-}out_B$ and $inside\text{-}out_C$ $Na_VAe1/Sp1_{CTD}p$ tetramers, while S6 and the SF face the exterior. $Inside\text{-}out_B$ is fourfold symmetric and has a wide cavity at the top of the structure, whereas $inside\text{-}out_C$ has a two-fold symmetric arrangement in which two of the diagonally opposed S5s are close to each other while the other two are far apart (Fig. 1d). Contrasting the $inside\text{-}out_A$ and $peripheral_{SF}$ forms, the individual PD monomers of the $inside\text{-}out_B$ and $inside\text{-}out_C$ bury substantially less surface against their neighbors than does the canonical Na_VAe1p structure (–329 and −448 $Å^2$, respectively) (Supplementary Table 1). The $Na_VAe1/Sp1_{CTD}p$ neck and coiled-coil regions form helices that are continuous with S6, similar to that observed in Na_VAb1p.

Remarkably, the individual PD subunits from these four non-canonical quaternary assemblies all have tertiary structures similar to those from canonical PD quaternary arrangements (Fig. 1a). There are some structural differences in the SF (Extended Data Fig. 2). The largest encompasses SF positions (+1) to (+3) in Ca_VSp1p and $Na_VAe1/Sp1_{CTD}$ and is centered around a dislocation of the (+2) tryptophan, which occupies its native position (Trp^{In}) in Na_VAb1p (Extended Data Fig. 2a) but is flipped out (Trp^{Out}) in Ca_VSp1p and $Na_VAe1/Sp1_{CTD}$ (Extended Data Fig. 2b,c). These differences suggest that, although the PD tertiary structure is independent of the quaternary assembly, attaining the SF native positions depends on quaternary interactions.

The dramatic differences in the PD quaternary structures of $Na_VAe1/Sp1_{CTD}$ relative to prior Na_VAe1p structures[11,18] (Fig. 1d,e) demonstrate that the same protein sequence, the Na_VAe1 PD, can adopt both inside-out (Fig. 1d) and canonical (Fig. 1e) quaternary structures and rules out the possibility that the non-canonical Na_VAb1p and Ca_VSp1p structures (Fig. 1b,c) are peculiar to those particular channels. Further, preservation of the Na_VAe1 PD tertiary fold in diverse quaternary contexts demonstrates that an individual PD can adopt multiple quaternary structures without losing its native tertiary structure. $Na_VAe1/Sp1_{CTD}$ $inside\text{-}out_B$ and $inside\text{-}out_C$ PD monomers bury substantially less surface area against their adjacent neighbors relative to the canonical Na_VAe1p form (Supplementary

Table 1). This fact eliminates the possibility that the native-like tertiary structure among the various non-canonical forms results from the non-canonical quaternary contacts. Together, our observations directly demonstrate that the tertiary structure of an individual PD, spanning S5–S6, is able to fold into a native-like structure independent of quaternary context and agree with the idea that intrasubunit interactions are the main determinants in the folding of PD tertiary structure[23].

VGIC-PD structural relatives occur in non-channel proteins.

The ability of the BacNa_V PD monomer to maintain a native-like tertiary structure independent of quaternary context prompted us to ask whether we could find this fold in other proteins. A DALI search[30,31] using the Na_VAe1p PD monomer (Pro148–Ser285) (Supplementary Data Set) identified this fold in essentially every VGIC superfamily channel member, including Na_V, Ca_V, and TRP channels (Fig. 2); channels whose pores resemble the VGIC superfamily, such as IP_3 receptors and glutamate receptors; and ion transport proteins, such as TRKA (Fig. 2). Remarkably, sequence identity with Na_VAe1p can be very low (such as 8% and 11% for GluR and TRPV1, respectively) and still yield the same core architecture of an antiparallel transmembrane helix pair bridged by a pore-helix-containing loop (Fig. 2). In all cases, the VGIC-PD monomer occurs in a tetrameric assembly. Owing to its VGIC superfamily predominance, we denote this as theVGIC-PD fold.

To our surprise, we identified many non-ion channel proteins with *Z* scores and $RMSD_{C\alpha}$s equivalent to VGIC superfamily members (for example *Z* score = ~6, TRPM2, Fig. 2). Most striking was an element from the plant-conserved region (PC-R) of rice (*Oryza sativa*) CesA8 cellulose synthase[32] (Fig. 2), consisting of an antiparallel helical pair bridged by a 25-residue α-helix-containing loop. Although sequence identity with Na_VAe1p is undetectable (3%), its structural similarity matches exemplar VGICs ($RMSD_{C\alpha}$ ~2.5–2.9 Å, Fig. 2), and agrees with prior analysis noting the similarity of this soluble enzyme element to Na_Vs[32]. Other good non-ion-channel structural matches are exemplified by the cytoskeletal protein SHROOM2 (ref. [33]), in which the antiparallel helix pair that matches Na_VAe1p is bridged by a loop bearing an antiparallel helical pair (Fig. 2), and chain Z of pea (*Pisum sativum*) photosystem II (PSII)[34], in which a short loop connects the transmembrane helical pair. Together, these observations indicate that VGIC-PD fold structural independence relies on transmembrane antiparallel helical pair association, a notion consistent with ideas regarding Kv pore monomer folding and prevalence of this feature in potassium channel PDs and coiled-coils[23].

S6-Neck hinge allows PD rigid body rearrangements.

The observed quaternary assembly diversity prompted investigation of how these unusual PD arrangements relate to each other and the canonical pore. Superposition of Na_VAb1p, Ca_VSp1p, Na_VAe1/Sp1$_{CTD}$p, and Na_VAe1p[18] PD monomer CTDs reveals that the different PD positions are interrelated by simple rigid body movements around a hinge at the S6-neck junction (Na_VAb1p His237, Ca_VSp1p Ala223, Na_VAe1p His245) (Fig. 3a). A rotation of ~45° in the membrane plane around this point connects the canonical Na_VAe1p and Ca_VSp1p inside-out$_{SF}$ (Fig. 3a,b). An additional ~60° tilt parallel to the membrane plane connects Ca_VSp1p inside-out$_{SF}$ and Na_VAb1p inside-out$_A$ (Fig. 3a,b). Na_VAe1/Sp1$_{CTD}$p

inside-out$_B$ and inside-out$_C$ forms are similarly related to the canonical conformation, involving the ~45° in membrane plane rotation followed by tilts of different degrees around an axis parallel to the membrane plane (Extended Data Fig. 3a,b).

Despite these extreme changes in PD quaternary structures, the CTDs superpose very well (Fig. 3c and Extended Data Fig. 3c). The Na$_V$Ab1p and Ca$_V$Sp1p neck domain cores comprise hydrophilic residues with ‘a’ and ‘d’ repeats that match the corresponding positions of Na$_V$Ae1p[18] (Fig. 3d–g). The main differences from Na$_V$Ae1p are that, in Na$_V$Ab1p, the neck N-terminal end near the S6 junction is slightly more open (Fig. 3f), and, in Ca$_V$Sp1p, the neck is one helical turn shorter than Na$_V$Ab1p and Na$_V$Ae1p (Fig. 3g,h and Extended Data Fig. 3d). The consistent neck domain packing patterns in structures that show different PD quaternary arrangements underscore that rigid body motions of the PD monomers around the S6-neck hinge connect the PD non-canonical arrangements.

Canonical CTDs support diverse quaternary assemblies.

To characterize the quaternary packing differences better, we used a distance-based analysis of the proximities of various channel elements relative to their neighbors. These contact plots identify extensive intersubunit interactions in the canonical PD quaternary structure at the P1–S6 interface, between adjacent SFs (SF–SF), and at the S6 cytoplasmic end where these helices form the intracellular gate[11,12,35] (Fig. 4a). Strikingly, none of the non-canonical forms show the quaternary P1–S6 or SF–SF contacts present in the canonical assembly (Fig. 4b–f). Instead, all non-canonical forms show close approaches of S5 and S6 to the neighboring subunit and to the diagonally placed subunit (Fig. 4a,b–f). Close quaternary contacts between S5 helices are found in Na$_V$Ab1p inside-out$_A$ (Fig. 4b) and Na$_V$Ae1/Sp1$_{CTD}$p inside-out$_C$ (Fig. 4e) and occur to a lesser extent in Na$_V$Ae1/Sp1$_{CTD}$p inside-out$_B$ (Fig. 4d) owing to the separation of the extracellular ends of the S5 helices. Such S5–S5 quaternary contacts are absent from the Ca$_V$Sp1p peripheral$_{SF}$ form (Fig. 4c). Instead, its S6 helices make extensive quaternary contacts that are not present in either the canonical or other non-canonical structures (Fig. 4a). In contrast to these extensive differences in PD quaternary interactions, the canonical and non-canonical forms share similar CTD intersubunit interactions in their neck and coiled-coil regions (Fig. 4). The lack of shared quaternary interactions among the various structures lends further support to the idea that the VGIC-PD is an autonomously folded monomeric unit whose tertiary structure is largely independent of quaternary interactions.

The VGIC-PD fold is conformationally stable in a bilayer.

Given the apparent stability of an isolated Kv PD monomer in a prior 650-ns MD simulation[23], we performed 3 independent 10-μs sMD simulations of an isolated BacNa$_V$ PD monomer to evaluate its behavior in a palmitoyl-oleoyl phosphatidylethanolamine (POPE) lipid bilayer. We chose Na$_V$Ae1p[18], because this PD has been observed in both canonical (Fig. 1e)[11,18] and non-canonical forms (Fig. 1d). Na$_V$Ae1p monomer backbone geometry remained highly constant for the entire simulation (RMSD$_{Cα}$ ~1.5 Å) (Fig. 5a). The S5–S6 antiparallel transmembrane helices and P1 helix were conformationally stable (RMSD$_{Cα}$ ~1.0 Å and ~0.4 Å, respectively), whereas, the SF and P2 helix were

more dynamic ($RMSD_{C\alpha}$ > 1.0 Å) (Fig. 5d,e) matching their behaviors in the various non-canonical quaternary forms.

The SF and S6 helix face the canonical tetramer central aqueous pore but face very different environments in the inside-out forms (Fig. 1f) and membrane-embedded monomer, raising questions about how these elements could be accommodated in the bilayer. The simulations show that the exposed SF polar groups sit at the lipid-water interface and are hydrated by ~15 waters within 3.0 Å (Fig. 5f,g) as well as by polar phospholipid head groups. Interestingly, the SF (+2) residue Trp199 is dynamic, and in one simulation (Replicate 2) samples the Trp^{In} position from canonical PD structures and a Trp^{Out} conformation similar to the one seen in $Na_VAe1/Sp1_{CTD}$ (Extended Data Figs. 2c and 4a). This dynamic behavior appears to be facilitated by interactions with the water sphere and bilayer hydrophilic groups and reinforces the idea that, unlike the VGIC-PD core, the SF structure needs quaternary interactions to stabilize its native conformation.

In contrast to the SF, the structure of the S6 transmembrane helix, which is primarily composed of nonpolar residues, remains indistinguishable from the canonical tetramer (Fig. 5b). Its two, pore-facing hydrophilic residues, Ser225 and Ser226, satisfy their hydrogen-bonding potential through interactions with backbone carbonyls from the previous helical turn in >80% of the simulation (Extended Data Fig. 4b,c), an interaction common to well-packed helical proteins[36–38]. Together, the simulations further support the idea that the VGIC-PD monomer is an autonomously folded unit that can adopt a stable, native-like, tertiary structure independent of quaternary interactions.

sFabs recognize the VGIC-monomer fold.

Phage display[8,39] synthetic Fab (sFab) selections using $Na_VAe1/Sp1_{CTD}p$ and Na_VAe1p incorporated into lipid nanodiscs[40] produced sFabs SAT09 and ANT05, respectively. Both yielded co-crystal structures with $Na_VAe1/Sp1_{CTD}p$ (Extended Data Fig. 5a–c and Table 1). sFab SAT09–$Na_VAe1/Sp1_{CTD}p$ crystals diffracted X-rays to 3.6 Å and were solved by molecular replacement. The structure shows that SAT09 recognizes the SF and surrounding P1 and P2 helices of PD monomer (Fig. 6a) that is essentially like that found in the canonical NaAe1p structure ($RMSD_{C\alpha}$ = 2.81 Å versus NavAe1p (PDB: 5HK7)[18]) (Extended Data Fig. 6a). sFab heavy and light chain residues make extensive contacts with the SF and P2 helix (Fig. 6b), forming a ~761-$Å^2$ interface. The center of these interactions is the conserved SF (+2) position, Trp199, which, along with the two subsequent SF residues, Ser200 and Met201, is incorporated into the P2 helix (Fig. 6b). This exposed Trp199 conformation is different from the canonical Na_VAe1p tetrameric pore (Fig. 6c) in which Trp199 in its Trp^{In} conformation is buried in the intersubunit interface and forms an anchor for the native SF conformation (Fig. 6d). However, it is similar to the Trp^{Out} conformation observed in the inside-out Na_VAe1 and $Sp1_{CTD}p$ structures (Extended Data Fig. 6b) and PD monomer simulations (Extended Data Fig. 4a). Hence, the data indicate that this conformation is not induced by the sFab but is a consequence of the sFab recognizing a conformation that is accessible in the absence of canonical intersubunit interactions.

The sFab SAT09–$Na_VAe1/Sp1_{CTD}p$ complex formed a decameric structure in the asymmetric unit comprising two head-to-head pentamers bridged by extensive inter-sFab

SAT09 interactions (Extended Data Fig. 6c). In this arrangement, individual PDs make very few interactions with other members of the complex and are oriented such that the SF faces the periphery (Extended Data Fig. 6d,e). As this pentameric assembly differs from other forms, we term it inside-out$_D$ (Extended Data Fig. 6e). Its S6 helix faces the central axis, but comparison with a monomer from the canonical Na_VAe1p[18] shows that the $Na_VAe1/Sp1_{CTD}p$ monomers are tilted by ~60° around the His245 S6-neck hinge (Extended Data Fig. 6f,g) and have a ~15° twist around the S6 axis. Similar to the other non-canonical $Na_VAe1/Sp1_{CTD}p$ quaternary arrangements, the individual inside-out$_D$ PD monomers bury substantially less surface area against their adjacent neighbors than does the canonical form (Supplementary Table 1), further supporting the idea that the native-like tertiary fold is essentially independent of quaternary structure. Contact analysis shows that, in contrast to the other forms, the PDs make very few intersubunit interactions, indicating that this quaternary arrangement is largely held together by interactions of the neck domain (Extended Data Fig. 6h). Notably, the coiled-coil region was not visible, suggesting that the crystallographic pentameric assembly is incompatible with its structure. Size-exclusion chromatography-multiangle light scattering (SEC-MALS)[41] (Extended Data Fig. 7a–c and Supplementary Table 2) of $Na_VAe1/Sp1_{CTD}p$ and the SAT09–$Na_VAe1/Sp1_{CTD}p$ complex shows that both are monodisperse tetramers, indicating that SAT09 does not affect oligomerization state. Hence, these data, together with the low degree of intersubunit contacts in the pentameric assembly, suggest that the pentameric form is a consequence of the crystallization conditions and not the result of SAT09 binding to the inside-out form.

The low-resolution ANT05–$Na_VAe1/Sp1_{CTD}p$ complex structure revealed a similar recognition mode where the sFab recognizes the exposed SF and P1 and P2 helices of an inside-out tetramer (Extended Data Fig. 8a). Although the resolution precludes detailed description interactions, it is clear that ANT05 is rotated ~90° along the sFab long axis relative to SAT09 (Extended Data Fig. 8b). This represents a different recognition mode of the structural epitope targeted by SAT09 and is consistent with the sequence differences between the SAT09 and ANT05 complementary-determining regions (CDRs) (Extended Data Fig. 5d). Notably, ANT05 was generated from selections using Na_VAe1p, a pore-only channel for which we have never observed non-canonical quaternary structures, even when the neck was disrupted and rendered flexible[18]. The fact that we were able to raise an sFab, ANT05, that recognizes a non-native quaternary structure using the natively assembled Na_VAe1p[18] as the target suggests that even very stable natively assembled pores can access non-canonical quaternary forms, and that these conformations are not rare.

SAT09 recognizes full-length BacNa$_V$s in multiple contexts.

Given our repeated observations of non-native quaternary structures in different BacNa$_V$ pore-only constructs, we wanted to probe whether such conformations could exist in a full-length channel. The SF (+2) Trp at the center of the epitope recognized by SAT09 is inaccessible in the canonical quaternary structure owing to its Trp^{In} conformation and burial in the intersubunit interface (Fig. 6d). Superposition of the SAT09–$Na_VAe1/Sp1_{CTD}p$ complex onto the canonical Na_VAe1p pore reveals that, even if the (+2) Trp could flip out to be exposed in the canonical conformation, SAT09 would make extensive clashes with the

surrounding subunits that would prevent it from binding to a canonical tetrameric BacNa$_V$ pore (Extended Data Fig. 9a). Thus we took advantage of the ability of SAT09 to bind to the exposed SF epitope to test whether it could bind to full-length BacNa$_V$s.

We first used fluorescence-detection size-exclusion chromatography (FSEC)[42] to test whether SAT09 could bind to detergent-solubilized C-terminal GFP fusions of three purified full-length BacNa$_V$s: Na$_V$Ae1, Na$_V$Sp1, and Na$_V$Ae1/Sp1$_{CTD}$ (Fig. 7a). For all three full-length channels, inclusion of SAT09 shifted the elution volume in a manner consistent with complex formation (Fig. 7b). Notably, we were not able to detect such a shift using K$_{2P}$2.1 (TREK-1)[43], a well-characterized potassium channel that lacks the SAT09 binding epitope (Extended Data Fig. 9b). Hence, these data indicate that SAT09 is able to recognize its SF epitope in a full-length channel and suggest that non-canonical pore conformation can be accessed in the presence of the VSD.

We next tested the ability of SAT09 to recognize full-length BacNa$_V$s in a lipid environment. Of the three channels that SAT09 could recognize in detergent, only Na$_V$Sp1 could be readily incorporated into soybean lipid nanodiscs. Because the size of Na$_V$Sp1–nanodisc complex would make it difficult to observe a substantial elution volume shift upon addition of the 50 kDa sFab, we adopted a different strategy to detect the interaction. We used Spycatcher[44] to make a covalent attachment between purified GFP bearing the SpyCatcher domain and an sFab SAT09 construct bearing an N-terminal SpyTag. We then used a combination of UV absorbance and FSEC to evaluate whether the purified GFP-tagged SAT09 could recognize Na$_V$Sp1 reconstituted into lipid nanodiscs (Fig. 7c). Comparisons of the UV absorbance profiles of the Na$_V$Sp1–nanodisc complex with the FSEC profiles run in the presence of SAT09-GFP show that SAT09 co-elutes with the nanodisc containing-fraction only when Na$_V$Sp1 is present (Fig. 7d), indicating specific recognition of the channel in a lipid environment. To investigate the SAT09-Na$_V$Sp1 interaction stoichiometry, we used SEC-MALS analysis. Because of difficulties analyzing nanodiscs using this method, we replaced the nanodics with the amphipol A8–35 (ref. [45]). These data reveal two monodisperse peaks for Na$_V$Sp1, one with a molecular mass matching a tetrameric channel and a higher molecular weight peak consistent with a dimer of channel tetramers (Extended Data Fig. 8c and Supplementary Table 2). Notably, the addition of SAT09 shifted both peaks to higher molecular weight species, with the peak containing the channel tetramer displaying a mass that was consistent with a stoichiometry of two SAT09 sFabs to one channel (Supplementary Table 2). These data indicate that it is possible to have at least two PD subunits in which the inside-out-like form is present in a full-length channel. Because binding the SAT09 epitope is incompatible with the native quaternary form (Extended Data Fig. 9a), our results indicate that inside-out like conformations can be accessed by some subunits in the full-length channel context.

Discussion

Our pore-only BacNa$_V$ studies yielded a surprising array of unconventional PD quaternary structures. The striking preservation of the native-like PD monomer structure in these diverse assemblies and in MD bilayer simulations supports the idea that the VGIC-PD fold can adopt its native tertiary structure independent of quaternary interactions and

agrees with prior inferences about $K_V1.3$ PD monomer stability based on cysteine labeling and simulation[23,24]. The independence of the VGIC-PD fold, which is built on a stable antiparallel helical pair, also aligns with ideas that many transmembrane domain structures are under thermodynamic control[46,47] and with the three-stage membrane-protein folding model in which helical pairs form and associate prior to assembly into the final native structure[26,27].

All VGICs require four PDs to make a functional ion-conducting pore assembled from either multiple, independent polypeptide chains, as for Kv[2] and TRP channels[3], or chains bearing multiple PDs, such as K_{2P} (ref. [6]), TPC[5], Ca_Vs[4], and Na_Vs[4]. The average eukaryotic protein synthesis rate is ~5.6 aa/sec[48,49] and sets a 'biogenic speed limit' for how quickly a cell can produce a protein of interest[48]. Hence, regardless of whether the PDs come from one or multiple polypeptides, there must be some period in which the PDs exist following their synthesis and membrane insertion prior to assembly with their final PD partners. For example, in a VGIC with 4 PDs within a single polypeptide, such as the sodium channel $Na_V1.4$, the shortest time between completion of the first (PD1) and fourth (PD4) PDs (spanning ~1,140 aa) is ~3.4 minutes. The time between completion of PD1 and the C-terminal ends of the other PDs is also substantial, being ~1 minute and ~2.8 minutes to the ends of PD2 and PD3, respectively. Although such time constraints are unlikely to affect VSDs as their self-contained four-helix bundle can fold independently[7–9], three of the four PDs would have to wait many minutes until they could adopt their final folded quaternary structure following PD4 synthesis. The observed ability of the VGIC-PD fold to adopt a native structure independent of quaternary context could be important for the maturation of the final VGIC native state and may help to protect unassembled PDs from being recognized as damaged or misfolded.

The observation that the sFab SAT09 binds to full-length channels, including Na_VSp1 reconstituted in membrane nanodiscs (Fig. 7b), indicates that non-canonical pore arrangements can be accessed in a full-length channel bearing VSDs in detergent and membrane environments. Prior electron paramagnetic resonance (EPR) studies of full-length Na_VSp1 and the pore-only Na_VSp1p noted substantial PD mobility differences between the two channels[15]. Residues reported to show the largest changes as well as enhanced lipid accessibility include three P1 pore helix residues that are buried in the canonical intersubunit interface but exposed in non-canonical conformations, including the Ca_VSp1p $peripheral_{SF}$ (Extended Data Fig. 10). Supported by the observation that the F170C P1 helix mutation enhanced slow inactivation, Chatterjee et al. interpreted the dynamic and lipid accessibility differences between Na_VSp1 and Na_VSp1p as indicative of a slow-inactivated conformation in Na_VSp1p[15]. On the basis of their exposure in Ca_VSp1p (Extended Data Fig. 10), it seems likely that these EPR parameter differences originate from non-canonical conformations. Whether such conformations are slow inactivated states remains unclear. The scale of these changes contrasts with the smaller, largely rigid body conformational changes in $BacNa_Vs$ PDs that have been suggested to represent an inactivated channel[50–52].

The canonical and non-canonical PD conformations are interrelated by simple rigid body displacements around a hinge in a CTD metastable element, the neck domain[18] (Fig. 3a–c). This property, together with sFab SAT09 binding data indicating that at least two PD

subunits can access non-canonical arrangements in a full-length channel raise the possibility that such non-canonical conformations impact function. Considered in the context of the PD mobility results of Chatterjee et al.[15], these observations also raise the possibility that the manifold of conformational states that underlies slow inactivation are richer than previously thought. The fact that we are able to crystallize various non-canonical forms and raise Fabs that recognize non-canonical quaternary forms demonstrates that such conformations are very stable. Whether and how this stability affects possible interconversion between non-canonical and canonical quaternary arrangements remains an open question.

The non-canonical tetrameric PD structures have conventionally assembled coiled-coil domains in their CTDs (Figs. 1 and 3d–f) and occur in both pore-only and full-length channels (Figs. 1 and 7). Two of these forms, peripheral$_{SF}$ and inside-out$_{A}$, bury more surface area than the canonical form (Supplementary Table 1), raising the question of whether such arrangements are intrinsic to the PD itself or are influenced by the CTD. Release of the CTD constraints does not preclude canonical PD quaternary structures, as canonical PD arrangements are observed in structures of Na$_{V}$Ae1p mutants with disordered neck domains but intact coiled-coils[18] and a *Magnetococcus* BacNa$_{V}$ pore-only construct lacking the coiled-coil[12]. Understanding the extent to which inter-PD interactions and the CTD influence non-canonical forms merits further study and will be important for understanding whether such non-canonical forms are favored in channels with coiled-coil-bearing CTDs, or can occur in other VGIC superfamily members lacking such structures.

Our observation of the robust, quaternary-structure-independent nature of the VGIC-PD tertiary fold sets a new framework for thinking about the fundamental structural units that comprise VGICs, their biogenesis, and possible evolutionary origins. Our data show that, similar to the other major functional unit in the VGIC transmembrane architecture, the VSD[7–9], the VGIC-PD tertiary fold can adopt a native-like structure without the requirement to be assembled into its final, functional tetrameric form. This independence may have relevance for the steps required to assemble a functioning VGIC from its constituent parts. Of note, the SF is the sole element that appears sensitive to quaternary interactions (Extended Data Figs. 2 and 4a). Further, disease-causing channel mutations may act by disrupting the stability of the VGIC-PD fold or its ability to partner with other subunits.

The notion of recurrent protein structural motifs continues to drive protein structure, design, and evolution studies[53,54]. Perhaps the most interesting insight from the demonstration of the VGIC-PD fold robustness is the consequence of this property for VGIC superfamily origins. The existence of structurally similar tertiary units in proteins that are not channels (Fig. 2) identifies the stable antiparallel helical pair as the key VGIC-PD structural element and suggests that oligomerization of an autonomously folded VGIC-PD followed by optimization of the interhelix loop containing the SF may have been important steps in the origin of the VGIC tetrameric pore. The observations we describe here should provide a starting point for studies of ion channel biogenesis, evolution, de novo design of novel channels, and the origins of poorly understood functional states.

Methods

DNA constructs.

Pore-only constructs for *Silicibacter pomeroyi* Ca_VSp1p, *Alkalilimnicola ehrlichii* Na_VAe1p, and *Alcanivorax borkumensis* Na_VAb1p are as described in ref. [10]. Full-length Na_VSp1 and Na_VAe1 were cloned from *Silicibacter pomeroyi* and *Alkalilimnicola ehrlichii* genomic DNA, respectively, into pET24b to create a fusion protein having in series, a tobacco etch viral (TEV) Protease site, green fluorescent protein (GFP), and His_6 tag at the C-terminal end. The Na_VAe1_{Sp1CTD} chimera is identical to that reported previously[18], with the Na_VAe1 transmembrane region, residues 1–241, joined to the Na_VSp1 CTD, residues 221–258. $Na_VAe1_{Sp1CTD}p$ spans Na_VAe1_{Sp1CTD} residues 142 to 258 and was cloned in a HM3C-LIC pET24b-derived vector[55], similar to the other pore-only constructs.

Protein expression and purification.

Expression and purification of Ca_VSp1p, Na_VAe1p, Na_VAb1p, and $Na_VAe1_{Sp1CTD}p$ was carried out as described in ref. [10]. The Na_VAb1p construct that lead to the highest resolution crystal structure had a double alanine deletion in the coiled-coil (ΔAla275/Ala276) that improved crystal packing. Proteins were expressed in *Escherichia coli* C41(DE3) grown in 2YT (5 g NaCl, 16 g tryptone, 10 g yeast extract) containing 25 μg/mL kanamycin. Cultures were inoculated with 1 mL/L of an overnight starter culture grown from a freshly transformed single colony and grown at 37 °C to an OD_{600} of 0.5, at which point the growth temperature was reduced to 18 °C. After ~30 minutes at 18 °C, cultures were induced by addition of isopropyl β-D-1-thiogalactopyranoside (IPTG) to 0.4 mM and grown for 52 hours. Cells were collected by centrifugation (6,000*g* at 4 °C). Cell pellets were frozen in liquid N_2 and stored at −80 °C. Frozen cell pellets were thawed on ice, resuspended in 250 mL cold lysis buffer (300 mM NaCl, 1 mM phenylmethylsulfonyl fluoride (PMSF), 50 mM Tris-HCl pH 8.0) and disrupted using an EmulsiFlex-C5 homogenizer (Avestin). Cell lysates were cleared from unbroken cells and debris by centrifugation (10,000*g* at 4 °C, 1 hour), and the supernatant was then ultracentrifuged (160,000*g* at 4 °C, 2 h) to pellet and separate the membranes from the supernatant, which was discarded. Membranes were homogenized in 50 mL of storage buffer (200 mM NaCl, 8% (vol/vol) glycerol, 20 mM Tris-HCl pH 8.0) with a Dounce Tissue Grinder (Kimble Kontes), frozen in liquid N_2 and stored at −80 °C. Frozen membranes were thawed on ice and extracted by addition of detergent in powder form, *n*-dodecyl-β-D-maltopyranoside (DDM, Anatrace) for Na_VAe1p and $Na_VAe_{Sp1CTD}p$ and *n*-decyl-β-D-maltopyranoside (DM, Anatrace) for Ca_VSp1p and Na_VAb1p, to a final concentration of 20 mM at 4 °C for 2 hours with gentle agitation. Detergent-solubilized membrane proteins were separated from insoluble material by ultracentrifugation (160,000*g* at 4 °C, 1 h), and the supernatant was collected.

Detergent extracted His-MBP-tagged proteins were applied to a 40 mL POROS MC 20 Ni^{2+} column (Applied Biosystems) equilibrated with buffer A (200 mM NaCl, 8% (vol/vol) glycerol, 1.5 mM DDM or 5 mM DM, 20 mM Tris-HCl pH 8.0). The column was washed with seven column volumes (CVs) of buffer A supplemented with 50 mM imidazole. The bound proteins were eluted by step application of buffer A supplemented with 300 mM imidazole over two CVs. The affinity tag was removed with an in-house purified His-tag-

labeled 3C protease[10] at ratio of 10:1 (wt/wt) fusion protein:protease at 4 °C for overnight with gentle agitation. The following day, imidazole was removed using a HiPrep 26/10 Desalting Column (GE Healthcare) preequilibrated with buffer A, and the cleaved protein was separated from the affinity tags and the protease by passing it through the POROS MC 20 Ni^{2+} column (Applied Biosystems) in tandem with a 20-mL amylose column (New England Biolabs) equilibrated in buffer A. The protein was concentrated to 15 mL using an Amicon Ultra-15 centrifugal filtration device (50-kDa MW cutoff, Millipore). The protein was diluted with a modified buffer A (8% (vol/vol) glycerol, 1.5 mM DDM or 5 mM DM, 20 mM Tris-HCl pH 8.0) to a final volume of 50 mL and a final NaCl concentration of 60 mM. The sample was loaded onto a 10-mL POROS HQ ion-exchange column (Applied Biosystems) equilibrated with buffer B (60 mM NaCl, 8% (vol/vol) glycerol, 1.5 mM DDM or 5 mM DM, 20 mM Tris-HCl pH 8.0). The protein was eluted by a linear gradient from 60 to 500 mM NaCl over 15 CVs, concentrated using an Amicon Ultra-15 centrifugal filtration device (50-kDa MW cutoff, Millipore) and applied to a Superdex 200 10/300 GL column (GE Healthcare) in buffer C (200 mM NaCl, 0.3 mM DDM or 2.7 mM DM, 20 mM Hepes pH 8.0). Sample purity was evaluated by SDS–PAGE stained with Coomassie brilliant blue R-250. Protein concentration was determined by absorbance at 280 nm using a Nanodrop 2000c spectrophotometer (Thermo Fisher Scientific).

Synthetic Fab selection and purification.

Synthetic Fabs (sFabs) were generated from a phage display library; the sorting procedure and selection are as described previously[56]. Briefly, His_6-MBP tagged[10] Na_VAe1p and Na_VAe1_{Sp1CTD} were reconstituted in eggPC:POPC (1:4) MSP 1D1[57] biotinylated nanodiscs. After removal of the empty nanodiscs via Ni-NTA purification, the biotinylation efficiency of nanodiscs was evaluated by pull-down on streptavidin-coated magnetic beads. Reconstituted $BacNa_Vs$ were used for phage library sorting using sFab Library E (kindly provided by S. Koide[58] based on described protocols[40]).

Single-point phage ELISA was used in the primary validation of binding affinities of generated sFabs in phage format as described previously[40]. Amplified phage particles at tenfold dilution were assayed against 20 nM biotinylated membrane proteins in nanodiscs using horse radish peroxidase (HRP)-conjugated anti-M13 monoclonal antibody (GE Healthcare, no. 27–9421-01). Assays were performed in library sorting buffer (200 mM NaCl, 25 mM Hepes, pH 8.0) supplemented with 2% BSA. Each sFab clone with A_{450} signal above 0.2 (three times the average background level of the assay) was sequenced, and unique sFabs were subcloned into pSVF4 or pIPTG vectors.

Expression and purification of SAT09 and ANT05 H12 sFabs were carried out as described in ref. [59]. The ANT05 H12 variant was derived from ANT05 using a strategy to reduce flexibility in the ‘elbow’ linker region between the Fab variable and constant domains[60]. This variant replaces the heavy chain $V^{111}SSASTKG^{118}$ sequence with $V^{111}FN\text{-}QIKG^{118}$, which bears both mutations and a deletion. The dash indicates the position of the deleted residue.

In brief, sFabs were expressed in *Escherichia coli* BL21 Gold grown in 2YT containing 100 μg/mL ampicillin at 37 °C to OD_{600nm} = 0.8, and expression was induced with 1 mM IPTG at 37 °C for 4 hours. Cells were collected, flash-frozen in liquid N_2 and stored at −80 °C.

For sFab purification, pellets were resuspended in 100 mL of PBS (500 mM NaCl, 20 mM sodium phosphate, pH 7.4), supplemented with 10 μg/mL DNase I, 0.5 mM $MgCl_2$ and 1 mM PMSF. Cell lysis was performed with a high-pressure homogenizer EmulsiFlex-C5 (Avestin) and the lysate was incubated for 20 minutes at 60 °C to precipitate endogenous proteins and Fab degradation products. Lysate was cooled down on ice and ultracentrifuged at 160,000*g* for 1 hour at 4 °C and loaded onto a 5 mL Protein A (GE Healthcare) column equilibrated with PBS. Column was washed with 10 CVs of PBS and protein was eluted with 2 CVs of 100 mM acetic acid. The elution sample was directly loaded onto a 20 mL Poros HS column (Applied Biosystems) packed in house for cation-exchange chromatography. The column was washed with 5 CVs of 50 mM sodium acetate pH 5, and the Fab was eluted by a linear gradient from 0 to 1 M NaCl. Fractions containing the eluted protein were loaded onto a HiPrep desalting column (GE Healthcare) equilibrated with PBS. Fabs were concentrated to 20 mg/mL, flash-frozen in liquid N_2 and stored at −80 °C.

Reconstitution of Na_VSp1 in nanodiscs.

Na_VSp1 expression and membrane preparation was performed as described for $BacNa_Vs$ pores. Frozen membranes were thawed on ice and extracted by addition of solid *n*-dodecyl-β-D-maltopyranoside (DDM, Anatrace) to a final concentration of 20 mM at 4 °C for 2 hours with gentle agitation. Detergent-solubilized membrane proteins were separated from insoluble material by ultracentrifugation (160,000*g* at 4 °C, 1 hour), and the supernatant was collected.

Detergent-extracted His-MBP-Na_VSp1 was applied to a 40 mL POROS MC 20 Ni^{2+} column (Applied Biosystems) equilibrated with buffer A (200 mM NaCl, 8% (vol/vol) glycerol, 1.5 mM DDM, 20 mM Tris-HCl, pH 8.0). The column was washed with seven column volumes (CVs) of buffer A supplemented with 50 mM imidazole. The bound protein was eluted by step application of two CVs of buffer A supplemented with 300 mM imidazole. The eluted protein fractions were concentrated to ~12 mL using an Amicon Ultra-50 centrifugal filtration device (100-kDa MW cutoff, Millipore) and loaded onto a HiPrep Desalting column 26/10 (GE Healthcare) to remove the imidazole. The protein was concentrated to 85 μM and mixed with purified MSP2N2 (expressed and purified as described in ref. [61]) and soybean lipid extract (Avanti Polar Lipids) in a 1:1:150 molar ratio. Following incubation at 4 °C for 1 hour, Biobeads (Biorad) that had been prewashed (30 minutes in methanol, 30 minutes in water, followed by 30 minutes in 200 mM NaCl, 20 mM Tris-HCl, pH 8.0) were added to the mixture, and the sample was incubated at 4 °C for 1 hour. To ensure nanodisc formation and complete removal of detergent Biobeads were replaced after 1 hour, and the sample was incubated overnight. The following day, the sample was recovered by carefully pipetting to avoid the Biobeads and loaded onto a 10-mL amylose gravity column. The column was washed with 10 CV of a buffer containing 200 mM NaCl, 20 mM Tris-HCl, pH 8.0. Purified 3C protease[10] was added overnight at 4 °C to achieve on-column cleavage. The following day, the flow-through containing Na_VSp1 reconstituted in nanodiscs

was collected, concentrated to a volume of 500 µL using an Amicon Ultra-50 centrifugal filtration device (100-kDa MW cutoff, Millipore), loaded onto a Superose 6 30/100 gel filtration column and relevant fractions were collected for FSEC assay.

Generation of GFP-fused SAT09 Fab.

We used the SpyTag-SpyCatcher system[44] to create a GFP-tagged SAT09 Fab for FSEC assays. The SpyTag was inserted at the SAT09 N terminus just after the periplasm export sequence, and the modified SAT09 was expressed as above for untagged SAT09. GFP was fused to the C termini of the SpyCatcher sequence subcloned in pDEST14 (Addgene plasmid no. 35044) and expressed in *E. coli* BL21 (DE3). Briefly, 2 L of 2YT medium supplemented with 100 µg/mL ampicillin was inoculated with 20 mL of an overnight starter culture grown from a freshly transformed single colony and incubated at 37 °C, 200 r.p.m. until OD_{600nm} = 0.5. The incubation temperature was lowered to 30 °C, and 0.5 mM IPTG was added to induce protein expression. After 3 hours, cells were collected by centrifugation (6,000*g*, 4 °C, 30 minutes). After sonication debris were removed by ultracentrifugation (160,000*g* at 4 °C, 1 hour), and the supernatant was loaded onto a 40-mL POROS MC 20 Ni^{2+} column (Applied Biosystems) equilibrated with buffer B (300 mM NaCl, 50 mM Tris-HCl, pH 8.0). The column was washed with 5 CVs of buffer B supplemented with 50 mM imidazole. The bound protein was eluted by step application of buffer B supplemented with 300 mM imidazole over two CVs. Then, 25 µM of purified SpyCatcher-GFP was mixed with excess purified SpyTag-SAT09 (1:1.5) and incubated at 4 °C for 1 hour and loaded on a HiPrep Desalting Column (GE Healthcare) equilibrated with 10 mM NaCl, 10 mM Tris-HCl, pH 8.0 to lower the salt concentration. The complex was purified by ion-exchange on a 4mL-PorosQ equilibrated in 10 mM NaCl, 10 mM Tris-HCl, pH 8.0 and eluted over a gradient of 20 CVs to a final concentration of 500 mM NaCl. The sample was loaded on a HiPrep Desalting Column (GE Healthcare) equilibrated with 200 mM NaCl, 10 mM Tris-HCl, pH 8.0, flash-frozen in liquid N_2, and stored at −80 °C.

FSEC and SEC-MALS assay.

Na_VSp1, Na_VAe1 and $Na_VAe1Sp1CTD$ with a C-terminal GFP tag subcloned in pET24b were transformed in *E. coli* C41 (DE3) for small-scale expression to test the binding of SAT09 with fluorescent size-exclusion chromatography (FSEC)[42]. Small-scale expression followed the same protocol described for the purification of $BacNa_Vs$ pores, with the difference being that only 50 mL of culture was inoculated for protein expression. Following sonication, cell membranes were isolated by ultracentrifugation (160,000*g*, 2 hours, 4 °C), resuspended in a solubilization buffer containing 200 mM NaCl, 10 mM DDM, 20 mM Hepes, pH 8, and were incubated for 2 hours at 4 °C. The suspension was ultracentrifuged (160,000*g*, 1 hour, 4 °C) and loaded onto a Superose 6 10/300 connected to a Shimadzu LC-20AD system having an RF-10XL fluorescence detector and SPD-20A UV/Vis detector. Elution profiles of full-length channels were compared with profiles of samples where each channel was incubated with SAT09-GFP overnight at 4 °C. As control, the experiment was performed on an unrelated ion channel, $K_{2P}2.1_{cryst}$ (TREK-1), that was expressed purified as described previously[43].

In order to test SAT09-GFP binding on Na_VSp1 reconstituted in nanodisc, we observed the shift in molecular weight of the fluorescent Fab that co-eluted with the channel, confirming the formation of the Fab–channel complex. For each run, 1.1 nmol of reconstituted channel was incubated with 1 nmol of Fab. These amounts were empirically determined to ensure good noise-to-signal ratio, avoiding saturation of fluorescent signal of unbound Fab. As a negative control, 2.2 nmoles of empty nanodisc were incubated with 2 nmoles of SAT09-GFP.

For amphipol reconstitution, Na_VSp1 purified in DDM was mixed in a 1:3 ratio (wt/wt) with amphipol A8–35 (Anatrace) and gently rotated for 3 hours at 4 °C. Detergent was removed by the addition of 15 mg of prewashed Biobeads (Biorad) per mL of reaction. The reaction was incubated at 4 °C overnight, and the sample was purified by SEC onto a Superose 6 equilibrated in 20 mM Tris, 200 mM NaCl, pH 8.

Multiangle light scattering (MALS) experiments were carried out at 4 °C using an HPLC (Shimadzu) with UV detector (SPD-20A) connected to a miniDAWN TREOS MALS detector and an Optilab T-rEX refractometer (Wyatt Technology). One hundred microliters of purified sample at 1 mg/mL was injected onto a Superose 6 Increase column (GE Healthcare). Buffer composition was 0.3 mM DDM, 200 mM NaCl, 20 mM Hepes, pH 8.0, for $Na_VAe1_{SpCTD}p$ and 200 mM NaCl, 20 mM Tris, pH 8.0, for Na_VSp1 in A8–35. Molecular weight was calculated at each time point during elution using a combination of UV absorbance, light scattering, and differential refractive index measurements with the Astra software package (Astra 6.0, Wyatt Technology). Conjugated analysis was performed using a *dn/dc* value of 0.143 for DDM and 0.15 for A8–35.

Protein crystallization and structure determination.

Crystallography.—For all the crystallization trials and crystal optimization, $BacNa_Vs$ pores were expressed and purified as described above. Seleno-methionine-labeled proteins (Ca_VSp1, Na_VAb1, $Na_VAe1_{Sp1CTD}p$) were expressed following the metabolic inhibition protocol[62]. Owing to general lower expression levels of Seleno-methionine-labeled proteins, each purification required 6 L cultures and yielded around 20 μL at 7.5–10 mg/mL. Purification was carried out as described above with the addition of 1 mM tris(2-carbossietil)phosphine (TCEP) in each purification buffer.

Ca_VSp1p.—Ca_VSp1p purified in DM as described above was concentrated to 13 mg/mL and reconstituted in bicelles[63] prior crystallization to a final bicelle concentration of 8%. Native crystals grew in 25% PEG4000, 200 mM $MgCl_2$, 100 mM MES, pH 6.5. To determine the three-dimensional structure, crystals of Seleno-methionine-labeled Ca_VSp1p were obtained from seeding with native crystals in the same crystallization condition.

Na_VAb1p.—Seleno-methionine-labeled NavAb1 purified in DM was concentrated to 13 mg/mL and crystallized in 3% PEG300, 0.75 M ammonium sulfate.

$Na_VAe1_{Sp1CTD}p$–SAT09 complex.—Purified $Na_VAe1_{Sp1CTD}p$ was incubated with a 1:1.5 molar excess of SAT09 Fab, and the complex was isolated by size-exclusion chromatography using a Superdex 200 (200 mM NaCl, 0.3 mM DDM, 20 mM Hepes

pH 8.0) and concentrated to 22–23 mg/mL. Crystals grew at 20 °C in 12– 14% PEG4000, 0.1 M NaCl, 0.1 M $MgCl_2$, 1 M Na acetate, pH 3.2–3.6. Crystals were collected at 4 °C by adding a cryoprotectant solution containing 17% PEG4000, 1 mM DDM, 0.1 M NaCl, 0.1 M $MgCl_2$, 0.1 M Na acetate, pH 3.6 and 5%-increasing steps of glycerol to a final concentration of 25%.

$Na_VAe1_{Sp1CTD}p$–ANT05 complex.—Purified $Na_VAe1_{Sp1CTD}p$ was incubated with a 1:1.5 molar excess of ANT05 Fab, and the complex was isolated by size-exclusion chromatography on a Superdex 200 (200 mM NaCl, 0.3 mM DDM, 20 mM Hepes, pH 8) and concentrated to 36 mg/mL. Crystals grew at 20 °C in 13% PEG4000, 2% propanol, 0.1 M $LiSO_4$, 0.1 M 2-[(2-amino-2-oxoethyl)-(carboxymethyl) amino]acetic acid (ADA), pH 6.5. Crystals were collected at 4 °C by adding a cryoprotectant solution containing 13% PEG4000, 2% propanol, 1 mM DDM, 0.1 M $LiS0_4$, 0.1 M ADA pH 6.5, and 5%-increasing steps of glycerol to a final concentration of 25%.

$Na_VAe1_{Sp1CTD}p$.—Purified $Na_VAe1_{Sp1CTD}p$ was concentrated to 13–13.5 mg/mL and crystallized in 22% PEG3350, 0.3 M KI, 8 mM sarcosine. Crystals were collected in 30% PEG3350, 0.3 M KI, 8 mM sarcosine and 1 mM Fos-choline 12 (FC-12), Anatrace). The FC-12 was added in order to remove the skin covering each crystal, leading to higher diffraction. Seleno-methionine-containing crystals diffracted at higher resolution than the native ones and were used for structure determination.

Structure determination.—All crystallographic data were collected at 100 K at the following wavelengths: Ca_VSp1p and Na_VAb1p (detergent and bicelles), 1.11587 Å; $Na_VAe1_{Sp1CTD}p$, 0.97954 Å; $Na_VAe1_{Sp1CTD}p$–SAT09, 1.03319 Å; $Na_VAe1_{Sp1CTD}p$–ANT05, 0.97790 Å.

Ca_VSp1p and Na_VAb1p.

Data from both native and seleno-methionine-derived crystals were collected at the Advanced Light Source Beamline 8.3.1, Lawrence Berkeley National Laboratory. Two- and three-wavelength MAD datasets were collected for the seleno-methionine crystals using the selenium peak and inflection, or peak, inflection, and remote wavelengths for Ca_VSp1p and Na_VAb1p, respectively. Diffraction images were integrated using iMOSFLM 1.0.5 (ref. [64]), and scaled with SCALA (3.3.20)[65]. Initial experimental phases were determined using SHELXE[66]. An initial model was obtained by manual placing secondary structure elements and improved with iterative rounds of manual rebuilding with COOT[67] and refinement with Refmac (5.6.0117)[68].

$Na_VAe1_{Sp1CTD}p$–SAT09 complex and $Na_VAe1_{Sp1CTD}p$–ANT05 complex.

Diffraction data for $Na_VAe1_{Sp1CTD}p$–SAT09 and $Na_VAe1_{Sp1CTD}p$–ANT05 complexes were collected at the Advanced Photon Source Beamlines 23ID-B and 24ID-E, respectively. Data were processed with XDS[69], scaled and merged with Aimless[70]. Structures were solved by molecular replacement using the Fab fragment (PDB: 4XGZ and its stable H12 (ref. [71]) variant for the SAT09 and ANT05 complexes, respectively) as the search model. Several cycles of manual rebuilding, using COOT[67], and refinement using REFMAC5 (5.6.0117)[68]

and PHENIX[72] were carried out to improve the electron density map. For AeSpCTD–ANT05 complex, secondary structure and Ramachandran restraints together with fourfold NCS restraints and no side-chains were used to refine the final model.

Na_VAe1_{Sp1CTD} seleno-methionine.

Three MAD datasets corresponding to the peak, inflection and remote selenium wavelengths were collected at the Advanced Photon Source Beamlines 23ID-B. Data were processed with XDS. Unmerged data were submitted to the automated structure solution pipeline CRANK2 (ref. [73]) from the CCP4i2 interface to determine initial experimental phases. An initial model was obtained by manual placing secondary structure elements and improved with iterative rounds of manual rebuilding with COOT and refinement with Refmac (5.6.0117)[68]. The full model was then refined to convergence in CNS[74,75] and PHENIX[72] using secondary structure and Ramachandran restraints together with fourfold NCS restraints and a higher resolution reference model (PDB: 5HK7).

Composite OMIT maps were generated with PHENIX[72].

Refinement information.

Ramachandran statistics were as follows (best/disallowed regions, %): Na_VAb1p (DM) (96.5/0.7), Na_VAb1p (bicelles) (97.7/0.1), Ca_VSp1p (bicelles) (92.3/1.2), $Na_VAe1/Sp1_{CTD}p$ (DDM) (82.8/1.6) $Na_VAe1/Sp1_{CTD}p$–SAT09 complex (94.1/0.2), $Na_VAe1/Sp1_{CTD}p$–ANT05 complex (87.9/1.9). Molprobity[76] scores were as follows (score, number of compared structures (N), compared resolution range, and percentile): Na_VAb1p (DM) (2.44, N = 4,562, 2.85 Å ± 0.25, 93), Na_VAb1p (bicelles) (2.14, N = 342, 3.50Å−3.90 Å, 100), Ca_VSp1p (bicelles) (2.18, N = 342, 3.50 Å ± 0.25, 100), $Na_VAe1/Sp1_{CTD}p$ (DDM) (2.96, N = 342, 3.25 Å−4.44 Å, 90) $Na_VAe1/Sp1_{CTD}p$–SAT09 complex (1.93, N = 4,562, 3.50Å−3.85 Å, 100), $Na_VAe1/Sp1_{CTD}p$–ANT05 complex (2.25, N = 342, 3.25 Å−4.75 Å, percentile: 100).

Molecular dynamics simulations.

System set up.—The coordinates for the Na_VAe1p monomer (residues 148–243) were obtained from chain A of the high-resolution (2.95 Å) crystal structure of the canonical tetrameric PD (PDB: 5HK7)[18]. The monomer was truncated after residue 243 and the C terminus was amidated to capture the transmembrane region only; the N-terminal proline was not modified further. All residues were assigned their standard protonation states at pH 7. Using the CHARMM-GUI webserver[77], the monomer was embedded in a palmitoyl-oleoyl phosphatidylethanolamine (POPE) bilayer and hydrated with a minimum water height of 20 Å above and below the membrane. Na^+ ions were added to neutralize, and the NaCl concentration was brought to 150 mM. Three independent monomer systems were prepared for simulation, with 31,712 total atoms for system 1, 31,766 for system 2, and 31,762 for system 3. All systems were converted to the Amber format with a combination of in-house scripts and the Amber LEaP program in AmberTools 16 (ref. [78]).

Simulation protocol.—Three independent atomistic MD simulations were performed with the Amber ff14SB protein force field and the lipid17 lipid force field parameter

sets[79,80]. Water molecules were described using the TIP3P model[81]. Simulations were carried out on GPUs with the PMEMD MD engine[82]. The protein heavy atoms and lipids were restrained with a harmonic potential and force constant of 5 kcal/(mol/Å^2). All systems were energy minimized for 10,000 steps, 2,500 steps of steepest descent followed by 7,500 steps of conjugate gradient. For NVT equilibration, the systems were gradually heated from 0 to 310 K over 300 ps. Temperature was maintained with the Langevin thermostat with a friction coefficient of γ = 1 / ps. Once a temperature of 310 K was reached, the systems were switched to NPT, and pressure was maintained at 1 atm using a semi-isotropic pressure tensor and the Monte Carlo (MC) barostat[83]. Protein and lipid restraints were gradually removed over the first 4 ns of equilibration. During the production period, the monomer systems were simulated for a total of 10.05 μs. Simulations were carried out under periodic boundary conditions. The SHAKE algorithm was used to constrain bonds involving hydrogen atoms enabling a 2-fs timestep[84]. The particle-mesh Ewald method was used to compute long-range electrostatics, and non-bonded interactions were cutoff at 12 Å with force-based switching between 10 Å and 12 Å, as suggested for membrane simulations employing the MC barostat[85]. The first 50 ns of equilibration for each simulation were excluded for subsequent analysis.

Simulation analysis.—All analysis of MD simulations was performed using the CPPTRAJ analysis package on AmberTools 16 (ref. [86]). Conformations were sampled from the trajectories every 200 ps. The C_α RMSD was calculated using the high-resolution crystal structure coordinates (PDB: 5HK7)[18] as a reference. Hydrogen bonds were defined as having acceptor and donor heavy atom (such as O–O distance in the case of a Ser-Phe sidechain to mainchain hydrogen bond) distances less than 3.0 Å and an angle between the acceptor heavy atom, the donor proton and the donor heavy atom greater than 135°. Hydrogen bonds were given a binary classification: present or not present.

Reporting summary.

Further information on research design is available in the Nature Research Reporting Summary linked to this article.

Extended Data

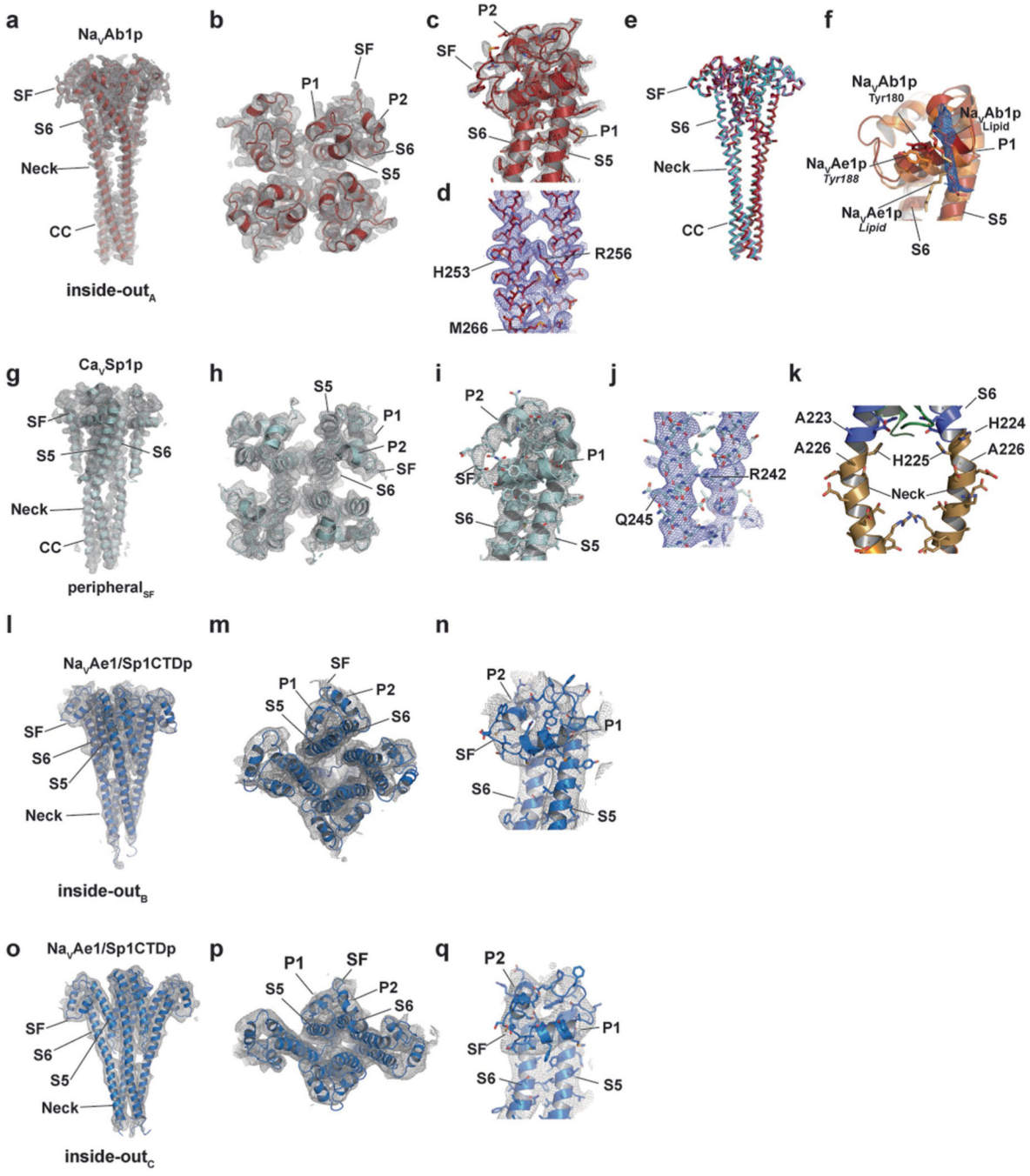

Extended Data Fig. 1 |. BacNa$_V$ PDs exemplar electron density and structural details.
a-c, 2Fo-Fc electron density (1σ) for Na$_V$Ab1p (firebrick) **a**, side view, **b**, extracellular view, and **c**, Single subunit. **d**, exemplar Na$_V$Ab1p Composite OMIT map density (1σ). **e**, Superposition of Na$_V$Ab1p structures determined in detergent (firebrick) and bicelles (cyan). **f**, Comparison of lipid bound to the P1 helix in Na$_V$Ab1p (firebrick) and Na$_V$Ae1p (PDB 5HK7)[18]. This lipid is modeled as phosphoenthanolamine and the 2Fo-Fo density

(1.0σ, marine mesh) shows a well-defined acyl chain sitting between the P1 and S6 helices of Na_VAb1p. **g-i**, 2Fo-Fc electron density (1σ) for Ca_VSp1p (cyan) **g**, side view, **h**, extracellular view, and **i**, Single subunit. **j**, exemplar Ca_VSp1p Composite OMIT map density (1σ). **k**, Close up of the Ca_VSp1p S6 (marine)-Neck (olive) junction showing two subunits. Select residues are indicated. **l-q**, 2Fo-Fc electron density (1σ) for $Na_VAe1/Sp1_{CTD}p$ (marine). **l-n**, inside-out_B tetramer **l**, side view, **m**, extracellular view, and **n**, single subunit. **o-q**, inside-out_C tetramer **o**, side view, **p**, extracellular view, and **q**, single subunit.

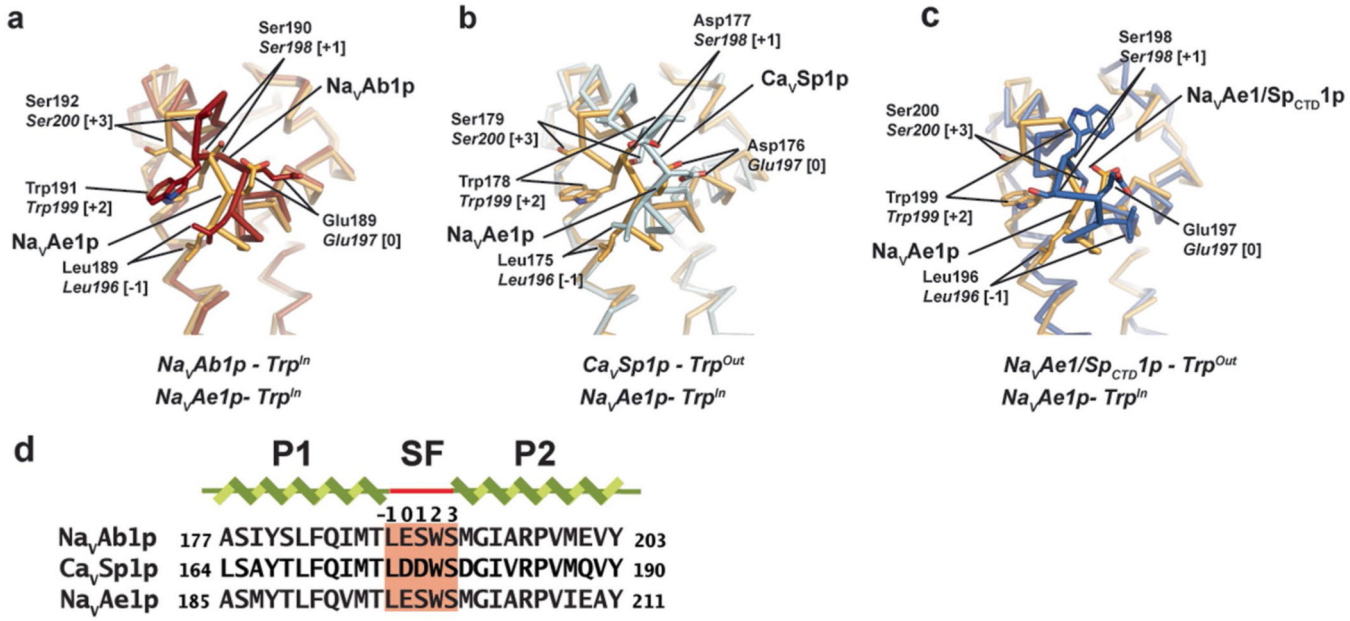

Extended Data Fig. 2 |. Structure comparison of selectivity filters from canonical and non-canonical quaternary assemblies.

a, Na_VAb1p (firebrick), **b**, Ca_VSp1p (cyan), and **c**, $Na_VAe1/Sp1_{CTD}p$ inside-out_C form(marine) compared with the Na_VAe1p canonical structure (orange) (PDB:5HK7)[18]. Selectivity filter Trp^{In} and Trp^{Out} conformations are indicated. **d**, Na_VAb1p, Ca_VSp1p, and Na_VAe1p sequence comparison. Residue numbers and positions of unified numbering scheme for the selectivity filter (SF) (−1 to +3) as defined by Shaya *et al.*[11] are shown.

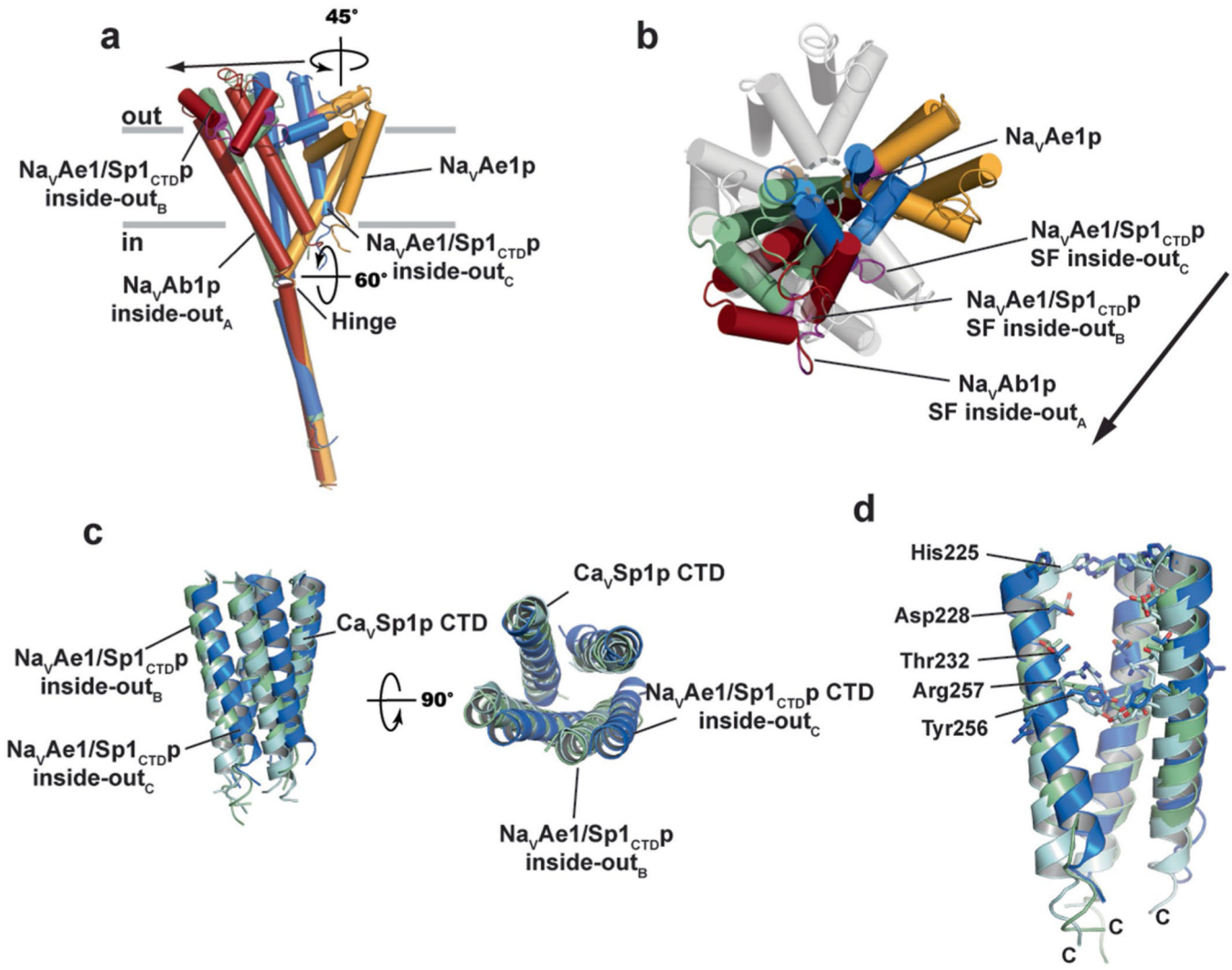

Extended Data Fig. 3 |. Structure comparison of inside-out and canonical quaternary assemblies. **a**, Superposition showing the rigid body movements that connect canonical Na_VAe1p (orange), inside-out$_A$ Na_VAb1p (firebrick), inside-out$_B$ $Na_VAe1/Sp1_{CTD}p$ (pale green), and inside-out$_C$ $Na_VAe1/Sp1_{CTD}p$ (marine) conformations. C-tails of each monomer are superposed. The selectivity filter of each monomer is magenta. All inside-out forms are related to Na_VAe1p by a 45° rotation round the hinge followed by varied degrees of translation indicated by the arrow. Rotation around the Hinge parallel to the membrane is indicated. **b**, extracellular view of 'a'. Location of central ion conducting pore is indicated by the open circle. Na_VAe1p tetramer is shown with one orange and three white subunits. Arrow shows the relationships among the inside-out forms**. c**, Superposition of the CTDs from $Na_VAe1/Sp1_{CTD}p$ inside-out$_B$ (pale green) and inside-out$_C$ (marine) conformations with Ca_VSp1p (cyan). **d**, Details of the central core from 'c'.

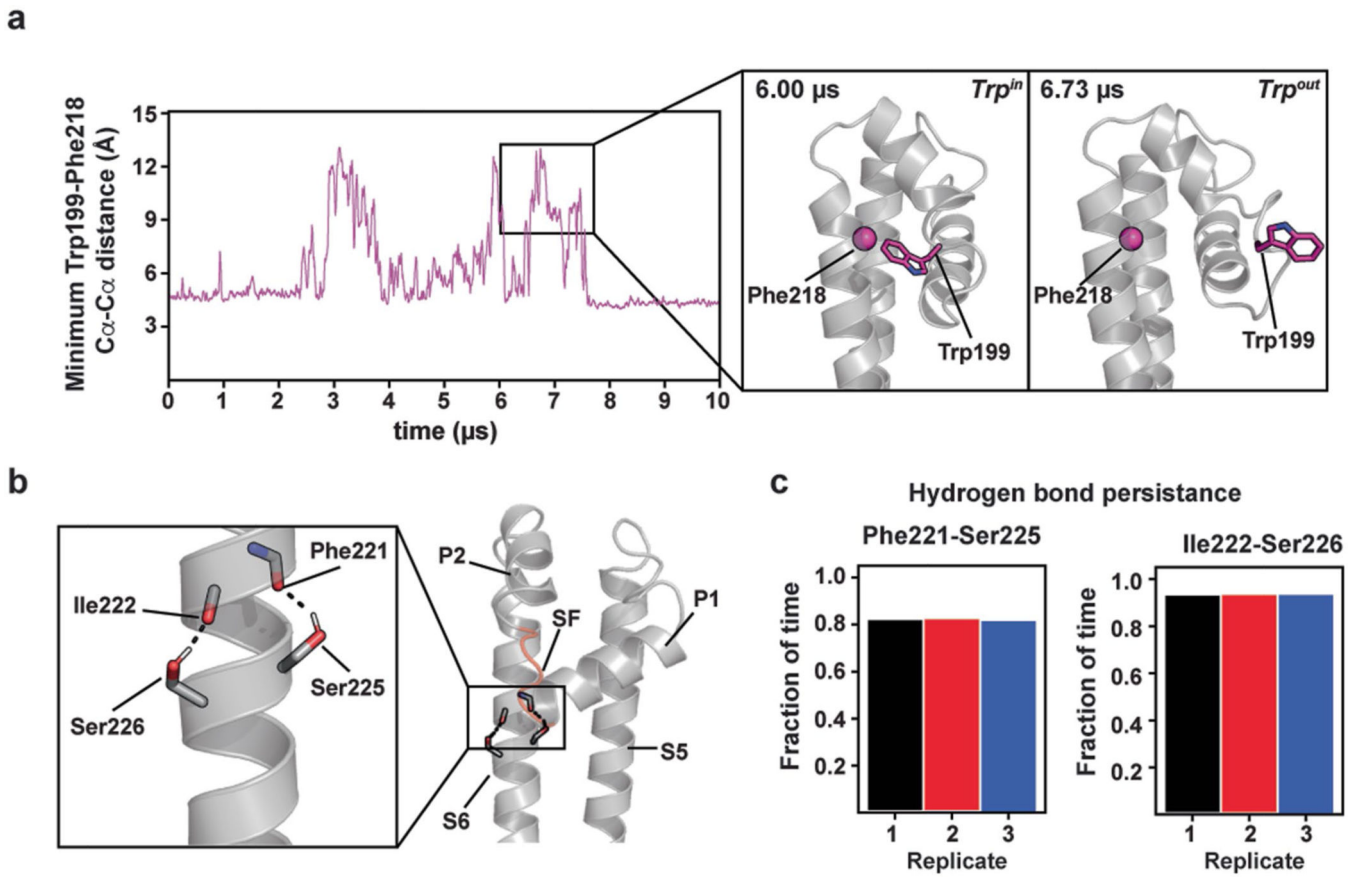

Extended Data Fig. 4 |. BacNa$_V$ pore loop and S6 hydrophilic residue dynamics.

a, Minimum distance between Trp199 and Phe218 C_α positions during simulation. Inset shows exemplar Trp199 (pink) Trp^{in} and Trp^{out} conformations at 6.00 μs and 6.73 μs, respectively. Pink sphere indicates Phe218 C_α. **b**, Ser225 and Ser226 hydrogen bond to the S6 helix backbone. **C**, Quantification of hydrogen bond persistence given as the proportion of time spent hydrogen bonded in each of three simulation replicates for the Phe211-Ser225 and Ile222-Ser226 pairs.

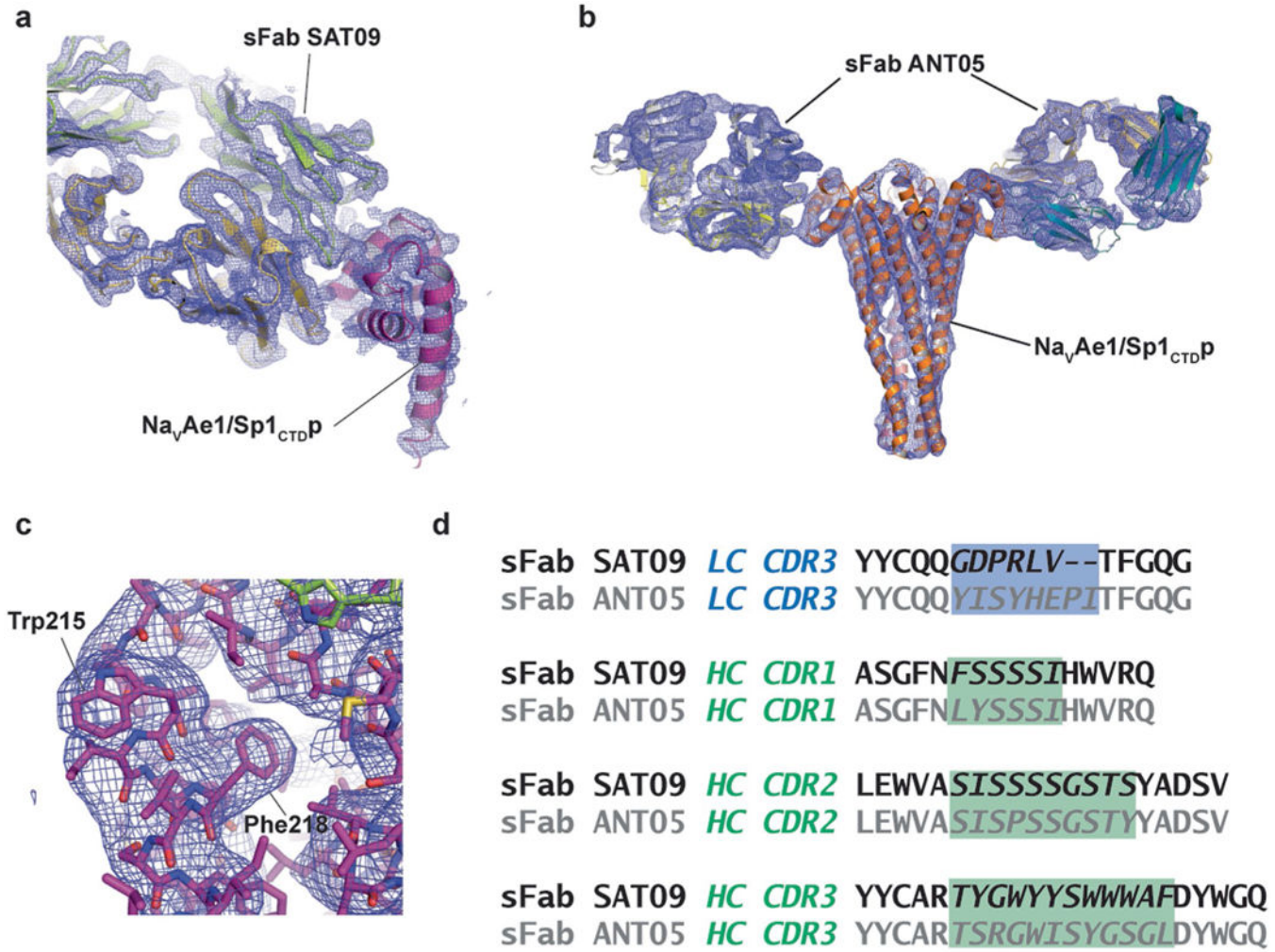

Extended Data Fig. 5 |. sFab:Na$_V$Ae1/Sp1$_{CTD}$p complexes.

a, 2Fo-Fc (2σ) electron density for sFab SAT09:Na$_V$Ae1/Sp1$_{CTD}$p. sFab SAT09 light (limon) and heavy (yellow orange) chains and Na$_V$Ae1/Sp1$_{CTD}$p (magenta) are indicated. **b**, 2Fo-Fc (1σ) electron density for sFab ANT05:Na$_V$Ae1/Sp1$_{CTD}$p. sFab ANT05 light (aquamarine) and heavy (yellow) chains and Na$_V$Ae1/Sp1$_{CTD}$p (orange) are indicated. **c**, Composite OMIT map density for SAT09:Na$_V$Ae1/Sp1$_{CTD}$p. Colors are as in '**a**'. **d**, Sequence comparisons of the light chain (LC) and heavy chain (HC) CDRs (blue and green, respectively) for sFabs SAT09 (black) and ANT05 (grey). CDR sequences are shown in italics.

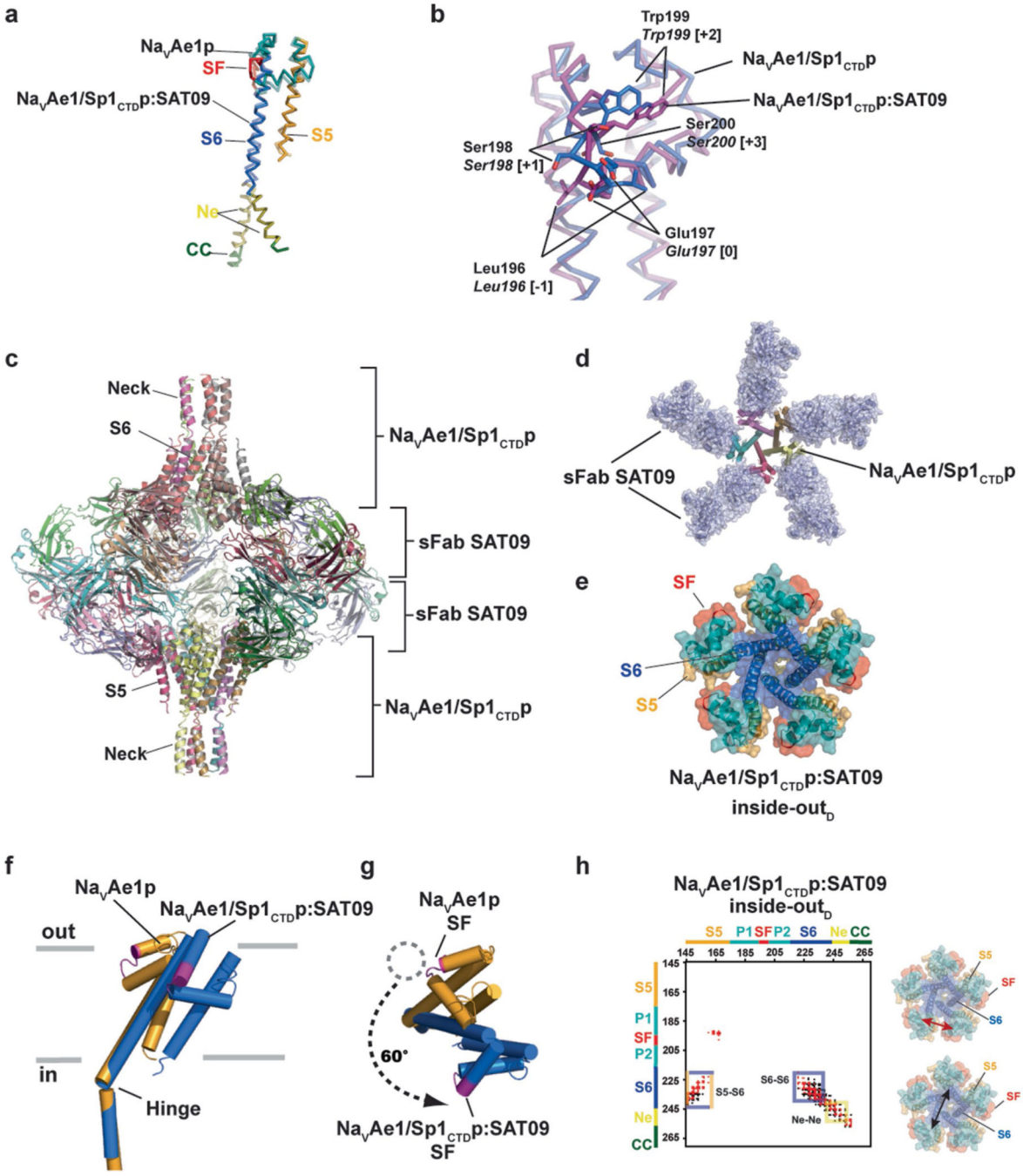

Extended Data Fig. 6 |. Structure of the sFabSAT09:$Na_VAe1/Sp1_{CTD}p$ complex.

a, Superposition of $Na_VAe1/Sp1_{CTD}p$ from the sFab SAT09:$Na_VAe1/Sp1_{CTD}p$ complex and Na_VAe1p from the canonical structure (PDB:5HK7)[18]. Channel elements are colored as follows, S5 (bright orange), SF (red), P1 and P2 helices (teal), S6 (marine), neck (olive) coiled-coil (forest). **b**, Superposition of $Na_VAe1/Sp1_{CTD}p$ (marine) and $Na_VAe1/Sp1_{CTD}p$ from the SAT09 complex (magenta). **c**, sFabSAT09:$Na_VAe1/Sp1CTDp$ complex asymmetric unit. **d**, extracellular view of a sFabSAT09:$Na_VAe1/Sp1CTDp$ pentameric complex (top). **e**, extracellular view of a $Na_VAe1/Sp1CTDp$ inside-out_D. Channel elements are colored as

in ‘A’. **f**, Superposition showing the rigid body movements that connect conformations of Na_VAe1p (orange) and $Na_VAe1/Sp1_{CTD}p$ from the sFabSAT09:$Na_VAe1/Sp1_{CTD}p$ complex (marine). C-tails of each monomer are superposed. The selectivity filter of each monomer is magenta. Hinge is indicated. **g**, extracellular view of ‘f’. Location of central ion conducting pore in Na_VAe1p is indicated by the open circle. Arrow shows the Na_VAe1p-$Na_VAe1/Sp1_{CTD}p$ relationship**. h**, sFabSAT09:$Na_VAe1/Sp1_{CTD}p$ complex contact map. C_α- C_α distances for (black) diagonal subunits at 20 Å and (red) neighboring subunits at 12 Å. Channel structural elements are indicated. extracellular views of the PDs having channel elements colored as in ‘a’ are shown. Arrows indicate the diagonal (black) and neighbor (red) distance relations of the contact plots.

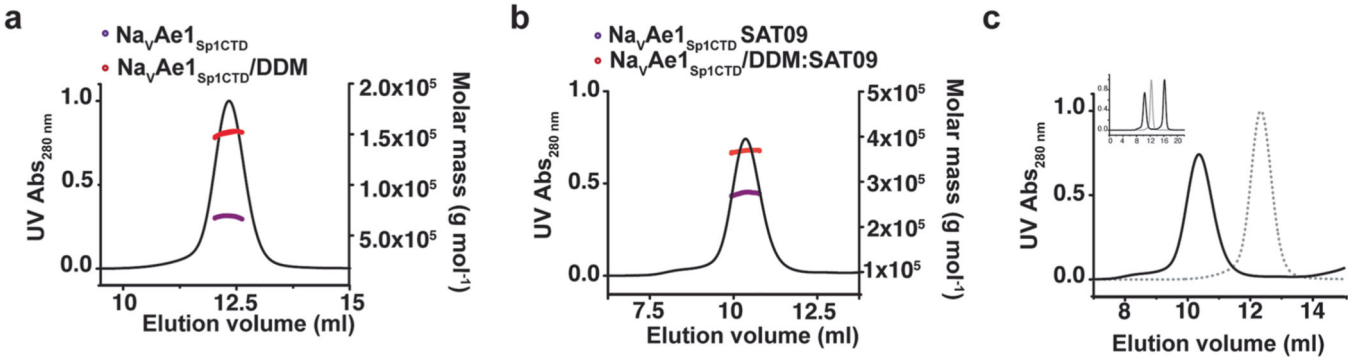

Extended Data Fig. 7 |. SEC-MALS analysis of Na_VAe1_{Sp1CTD} and SAT09:Na_VAe1_{Sp1CTD}.
a, SEC-MALS chromatograms of 15 μM Na_VAe1_{Sp1CTD} purified in DDM. **b**, SEC-MALS chromatograms of 15 μM Na_VAe1_{Sp1CTD} in complex with 2.5-fold excess of sFab SAT09. The red and purple lines represents respectively the total molar mass and protein molar mass fitting results. **c**, Superimposition of Na_VAe1_{Sp1CTD} and SAT09:Na_VAe1_{Sp1CTD} SEC-MALS chromatograms from ‘a’ and ‘b’. Chromatograms for ‘a’ and ‘b’ are available as source data.

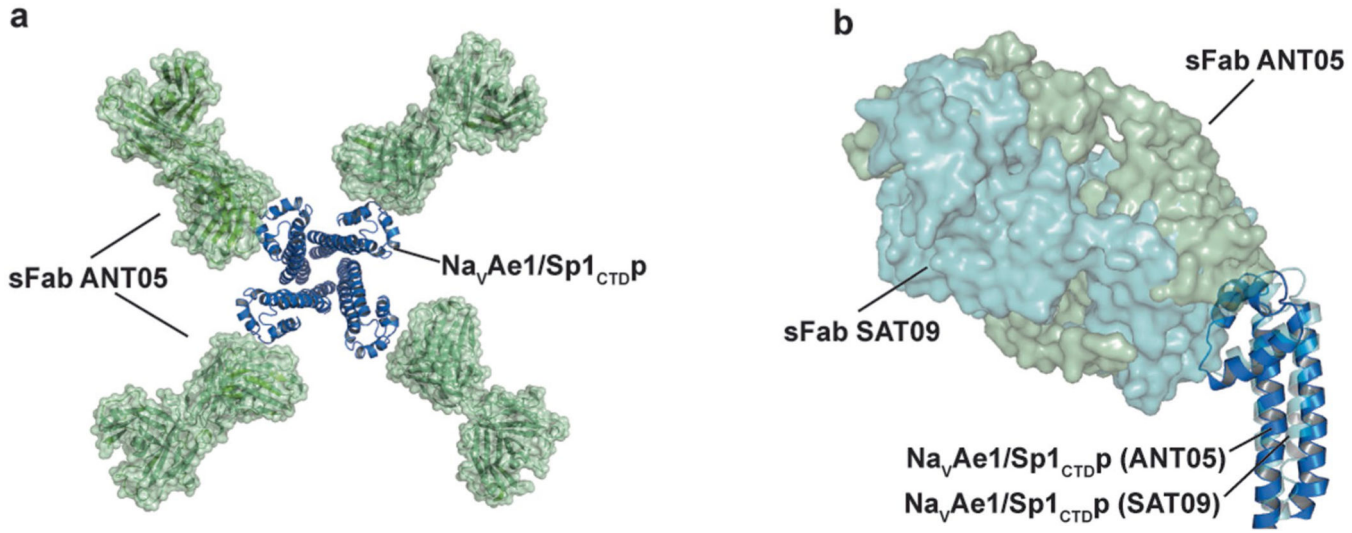

Extended Data Fig. 8 |. Structure of the sFabANT05:$Na_VAe1/Sp1CTDp$ complex.

a, extracellular view of the sFabANT05:$Na_VAe1/Sp1CTDp$ complex. sFabANT05 (green) is shown in cartoon and surface rendering. $Na_VAe1/Sp1CTDp$ (marine) is shown in cartoon rendering. **b**, Comparison of the binding modes of sFabANT05 (green) and sFabSAT09 (cyan) to $Na_VAe1/Sp1CTDp$. $Na_VAe1/Sp1CTDp$ from the sFabANT05 complex is marine. $Na_VAe1/Sp1CTDp$ from the sFabSAT09 complex is cyan.

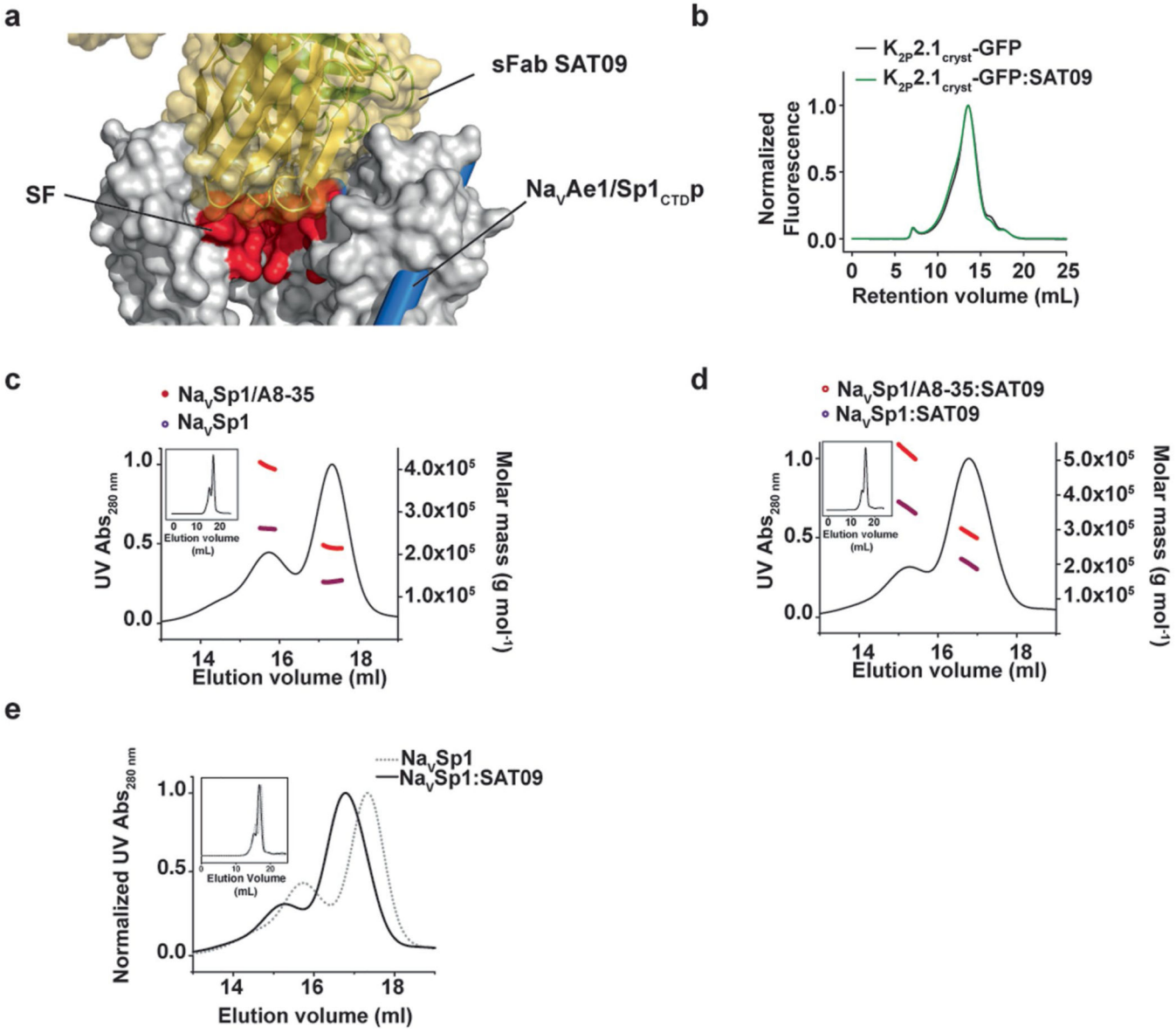

Extended Data Fig. 9 |. Characterization of sFab SAT09 binding.

a, Superposition of the sFabSAT09 complex (solid yellow, green SAT09 and marine cylinders $Na_VAe1/Sp1CTDp$ on the Na_VAe1p (space filling, white) canonical structure (PDB:5HK7)[18] showing three of the four subunits. Selectivity filter (SF) region of Na_VAe1p is colored red. **b**, Superose 6 10/300 FSEC profiles of $K_{2P}2.1(TReK\text{-}1)_{cryst}$-GFP alone (black) and with SAT09 (green). DDM-solubilized fraction from $K_{2P}2.1(TReK\text{-}1)_{cryst}$-GFP expressing *Pichia pastoris* cells (100 µl) was incubated with 1 nmol of sFab SAT09. **c**, SEC-

MALS chromatograms of 9 μM Na_VSp1 reconstituted in amphipol A8–35. **d**, SEC-MALS chromatogram of 9 μM Na_VSp1-SAT09 complex reconstituted in amphipol A8–35 and taken after purification of the complex on Superose 6. **e**, Superimposition of Na_VSp1 (dashed line) and SAT09:Na_VSp1 (black) SEC-MALS chromatograms from 'c' and 'd'. Chromatograms for 'b-e' are available as source data.

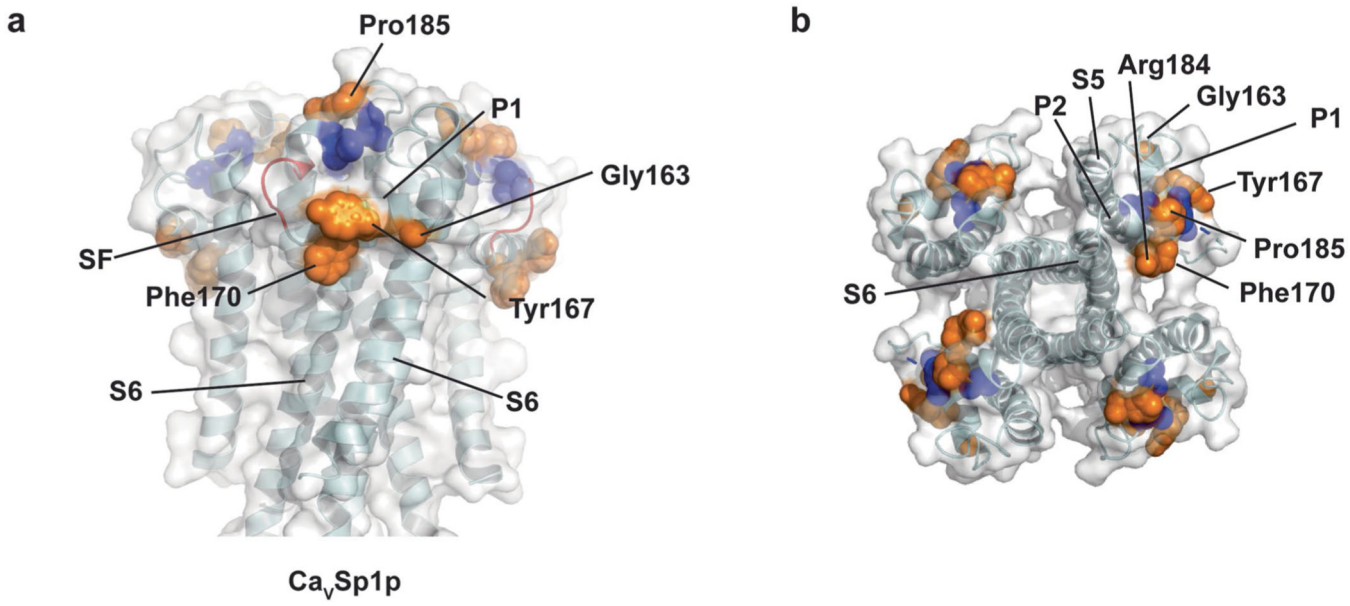

Extended Data Fig. 10 |. EPR mobility changes.

a, Side and **b**, extracellular views of the Ca_VSp1p structure showing residues having changed mobility relative to the full length channel. Increased (orange), decreased (blue). Selectivity filter is colored red. EPR data are from [15].

Supplementary Material

Refer to Web version on PubMed Central for supplementary material.

Acknowledgements

We thank K. Brejc, L. Jan, and T. Kortemme for comments on the manuscript; S. Wong for expert technical assistance in protein preparation. This work was supported by grants NIH-NHLBI R01-HL080050, NIH-NIDCD R01-DC007664, and the Program for Breakthrough Biomedical Research, which is partially funded by the Sandler Foundation to D. L. M., NIH-NIGMS R35 GM122603 to W. F. D., NIH-NIGMS R21-GM100224 and R01-GM137109 to M. G., NIH-NIGMS GM117372 to A. A. K., and an AHA postdoctoral fellowships to C. A. and M. L. This work is based on research conducted at the Northeastern Collaborative Access Team beamlines, which are funded by the National Institute of General Medical Sciences from the National Institutes of Health (Grant P30 GM124165). This research used resources of the Advanced Photon Source, a US Department of Energy (DOE) Office of Science User Facility operated for the DOE Office of Science by Argonne National Laboratory under Contract DE-AC02-06CH11357.

Data availability

Coordinates and structures factors for Na_VAb1p (DM), Na_VAb1p (bicelles), Ca_VSp1p (bicelles), $Na_VAe1/Sp1_{CTD}p$ (DDM), $Na_VAe1/Sp1_{CTD}p$-SAT09, and $Na_VAe1/Sp1_{CTD}p$-SAT09 are deposited in the RCSB under accession codes Na_VAb1p (DM) (PDB: 7PGG),

Na_VAb1p (bicelles) (PDB: 7PGI), Ca_VSp1p (bicelles) (PDB: 7PGF), $Na_VAe1/Sp1_{CTD}p$ (DDM) (PDB: 7PGH), $Na_VAe1/Sp1_{CTD}p$:SAT09 complex (PDB: 7PGB), and $Na_VAe1/Sp1_{CTD}p$:ANT05 complex (PDB: 7PG8). Source data are provided with this paper.

References

1. Yu FH & Catterall WA The VGL-chanome: a protein superfamily specialized for electrical signaling and ionic homeostasis. Sci. STKE 2004, re15 (2004).
2. Isacoff EY, Jan LY & Minor DL Jr Conduits of life's spark: a perspective on ion channel research since the birth of neuron. Neuron 80, 658–674 (2013). [PubMed: 24183018]
3. Zhao Y, McVeigh BM & Moiseenkova-Bell VY Structural pharmacology of TRP channels. J. Mol. Biol 433, 166914 (2021).
4. Catterall WA, Wisedchaisri G. & Zheng N. The chemical basis for electrical signaling. Nat. Chem. Biol 13, 455–463 (2017). [PubMed: 28406893]
5. Jin X. et al. Targeting two-pore channels: current progress and future challenges. Trends Pharmacol. Sci 41, 582–594 (2020). [PubMed: 32679067]
6. Natale AM, Deal PE & Minor DL Jr. Structural insights into the mechanisms and pharmacology of K2P potassium channels. J. Mol. Biol 433, 166995 (2021).
7. Chakrapani S, Sompornpisut P, Intharathep P, Roux B. & Perozo E. The activated state of a sodium channel voltage sensor in a membrane environment. Proc. Natl Acad. Sci. USA 107, 5435–5440 (2010). [PubMed: 20207950]
8. Li Q. et al. Structural mechanism of voltage-dependent gating in an isolated voltage-sensing domain. Nat. Struct. Mol. Biol 21, 244–252 (2014). [PubMed: 24487958]
9. Li Q, Wanderling S, Sompornpisut P. & Perozo E. Structural basis of lipid-driven conformational transitions in the KvAP voltage-sensing domain. Nat. Struct. Mol. Biol 21, 160–166 (2014). [PubMed: 24413055]
10. Shaya D. et al. Voltage-gated sodium channel (NaV) protein dissection creates a set of functional pore-only proteins. Proc. Natl Acad. Sci. USA 108, 12313–12318 (2011). [PubMed: 21746903]
11. Shaya D. et al. Structure of a prokaryotic sodium channel pore reveals essential gating elements and an outer ion binding site common to eukaryotic channels. J. Mol. Biol 426, 467–483 (2014). [PubMed: 24120938]
12. McCusker EC et al. Structure of a bacterial voltage-gated sodium channel pore reveals mechanisms of opening and closing. Nat. Commun 3, 1102 (2012). [PubMed: 23033078]
13. McCusker EC, D'Avanzo N, Nichols CG & Wallace BA A simplified bacterial "pore" provides insight into the assembly, stability and structure of sodium channels. J. Biol. Chem 286, 16386–16391 (2011). [PubMed: 21454659]
14. Payandeh J. & Minor DL Jr Bacterial voltage-gated sodium channels (BacNas) from the soil, sea, and salt lakes enlighten molecular mechanisms of electrical signaling and pharmacology in the brain and heart. J. Mol. Biol 427, 3–30 (2015). [PubMed: 25158094]
15. Chatterjee S. et al. The voltage-gated sodium channel pore exhibits conformational flexibility during slow inactivation. J. Gen. Physiol 150, 1333–1347 (2018). [PubMed: 30082431]
16. Saha SC et al. Characterization of the prokaryotic sodium channel NavSp pore with a microfluidic bilayer platform. PLoS ONE 10, e0131286 (2015).
17. Bagneris C. et al. Role of the C-terminal domain in the structure and function of tetrameric sodium channels. Nat. Commun 4, 2465 (2013). [PubMed: 24051986]
18. Arrigoni C. et al. Unfolding of a temperature-sensitive domain controls voltage-gated channel activation. Cell 164, 922–936 (2016). [PubMed: 26919429]
19. Naylor CE et al. Molecular basis of ion permeability in a voltage-gated sodium channel. EMBO J. 35, 820–830 (2016). [PubMed: 26873592]
20. Bagneris C. et al. Prokaryotic NavMs channel as a structural and functional model for eukaryotic sodium channel antagonism. Proc. Natl Acad. Sci. USA 111, 8428–8433 (2014). [PubMed: 24850863]

21. Deutsch C. Potassium channel ontogeny. Annu Rev. Physiol 64, 19–46 (2002). [PubMed: 11826262]
22. Deutsch C. The birth of a channel. Neuron 40, 265–276 (2003). [PubMed: 14556708]
23. Gajewski C, Dagcan A, Roux B. & Deutsch C. Biogenesis of the pore architecture of a voltage-gated potassium channel. Proc. Natl Acad. Sci. USA 108, 3240–3245 (2011). [PubMed: 21300900]
24. Delaney E, Khanna P, Tu L, Robinson JM & Deutsch C. Determinants of pore folding in potassium channel biogenesis. Proc. Natl Acad. Sci. USA 111, 4620–4625 (2014). [PubMed: 24616516]
25. McDonald SK, Levitz TS & Valiyaveetil FI A shared mechanism for the folding of voltage-gated K+ channels. Biochemistry 58, 1660–1671 (2019). [PubMed: 30793887]
26. Popot JL & Engelman DM Membrane protein folding and oligomerization: the two-stage model. Biochemistry 29, 4031–4037 (1990). [PubMed: 1694455]
27. Popot JL, Gerchman SE & Engelman DM Refolding of bacteriorhodopsin in lipid bilayers. A thermodynamically controlled two-stage process. J. Mol. Biol 198, 655–676 (1987). [PubMed: 3430624]
28. Shaya D. et al. Structure of a prokaryotic Sodium Channel Pore Reveals Essential Gating Elements and an Outer Ion Binding Site Common to Eukaryotic Channels. J. Mol. Biol 426, 467–483 (2013). [PubMed: 24120938]
29. Lupas AN & Gruber M. The structure of alpha-helical coiled coils. Adv. Protein Chem 70, 37–78 (2005). [PubMed: 15837513]
30. Holm L. & Laakso LM Dali server update. Nucleic Acids Res. 44, W351–W355 (2016). [PubMed: 27131377]
31. Holm L. & Rosenstrom P. Dali server: conservation mapping in 3D. Nucleic Acids Res. 38, W545–W549 (2010). [PubMed: 20457744]
32. Rushton PS et al. Rice cellulose synthaseA8 plant-conserved region is a coiled-coil at the catalytic core entrance. Plant Physiol. 173, 482–494 (2017). [PubMed: 27879387]
33. Zalewski JK et al. Structure of the shroom-rho kinase complex reveals a binding interface with monomeric shroom that regulates cell morphology and stimulates kinase activity. J. Biol. Chem 291, 25364–25374 (2016). [PubMed: 27758857]
34. Grinzato A. et al. High-Light versus low-light: effects on paired photosystem II supercomplex structural rearrangement in pea plants. Int. J. Mol. Sci 21, 8643 (2020). [PubMed: 33207833]
35. Payandeh J, Scheuer T, Zheng N. & Catterall WA The crystal structure of a voltage-gated sodium channel. Nature 475, 353–358 (2011). [PubMed: 21743477]
36. Mravic M. et al. Packing of apolar side chains enables accurate design of highly stable membrane proteins. Science 363, 1418–1423 (2019). [PubMed: 30923216]
37. Engelman DM & Steitz TA The spontaneous insertion of proteins into and across membranes: the helical hairpin hypothesis. Cell 23, 411–422 (1981). [PubMed: 7471207]
38. Baker EN & Hubbard RE Hydrogen bonding in globular proteins. Prog. Biophys. Mol. Biol 44, 97–179 (1984). [PubMed: 6385134]
39. Uysal S. et al. Crystal structure of full-length KcsA in its closed conformation. Proc. Natl Acad. Sci. USA 106, 6644–6649 (2009). [PubMed: 19346472]
40. Dominik PK & Kossiakoff AA Phage display selections for affinity reagents to membrane proteins in nanodiscs. Methods Enzymol. 557, 219–245 (2015). [PubMed: 25950967]
41. Folta-Stogniew E. Oligomeric states of proteins determined by size-exclusion chromatography coupled with light scattering, absorbance, and refractive index detectors. Methods Mol. Biol 328, 97–112 (2006). [PubMed: 16785643]
42. Kawate T. & Gouaux E. Fluorescence-detection size-exclusion chromatography for precrystallization screening of integral membrane proteins. Structure 14, 673–681 (2006). [PubMed: 16615909]
43. Lolicato M. et al. K2P2.1(TREK-1):activator complexes reveal a cryptic selectivity filter binding site. Nature 547, 364–368 (2017). [PubMed: 28693035]
44. Zakeri B. et al. Peptide tag forming a rapid covalent bond to a protein, through engineering a bacterial adhesin. Proc. Natl Acad. Sci. USA 109, E690–E697 (2012). [PubMed: 22366317]

45. Hesketh SJ et al. Styrene maleic-acid lipid particles (SMALPs) into detergent or amphipols: an exchange protocol for membrane protein characterisation. Biochim. Biophys. Acta Biomembr 1862, 183192 (2020).
46. Cymer F, von Heijne G. & White SH Mechanisms of integral membrane protein insertion and folding. J. Mol. Biol 427, 999–1022 (2015). [PubMed: 25277655]
47. Popot JL & Engelman DM Membranes do not tell proteins how to fold. Biochemistry 55, 5–18 (2016). [PubMed: 26649989]
48. Ingolia NT, Lareau LF & Weissman JS Ribosome profiling of mouse embryonic stem cells reveals the complexity and dynamics of mammalian proteomes. Cell 147, 789–802 (2011). [PubMed: 22056041]
49. Bostrom K. et al. Pulse-chase studies of the synthesis and intracellular transport of apolipoprotein B-100 in Hep G2 cells. J. Biol. Chem 261, 13800–13806 (1986). [PubMed: 3020051]
50. Payandeh J, Gamal El-Din TM, Scheuer T, Zheng N. & Catterall WA Crystal structure of a voltage-gated sodium channel in two potentially inactivated states. Nature 486, 135–139 (2012). [PubMed: 22678296]
51. Tang L. et al. Structural basis for inhibition of a voltage-gated Ca2+ channel by Ca2+ antagonist drugs. Nature 537, 117–121 (2016). [PubMed: 27556947]
52. Zhang X. et al. Crystal structure of an orthologue of the NaChBac voltage-gated sodium channel. Nature 486, 130–134 (2012). [PubMed: 22678295]
53. Mackenzie CO & Grigoryan G. Protein structural motifs in prediction and design. Curr. Opin. Struct. Biol 44, 161–167 (2017). [PubMed: 28460216]
54. Alva V. & Lupas AN From ancestral peptides to designed proteins. Curr. Opin. Struct. Biol 48, 103–109 (2018). [PubMed: 29195087]

References

55. Hammon J, Palanivelu DV, Chen J, Patel C. & Minor DL Jr A green fluorescent protein screen for identification of well-expressed membrane proteins from a cohort of extremophilic organisms. Protein Sci. 18, 121–133 (2009). [PubMed: 19177357]
56. Dominik PK et al. Conformational chaperones for structural studies of membrane proteins using antibody phage display with nanodiscs. Structure 24, 300–309 (2016). [PubMed: 26749445]
57. Denisov IG, Grinkova YV, Lazarides AA & Sligar SG Directed self-assembly of monodisperse phospholipid bilayer Nanodiscs with controlled size. J. Am. Chem. Soc 126, 3477–3487 (2004). [PubMed: 15025475]
58. Miller KR et al. T cell receptor-like recognition of tumor in vivo by synthetic antibody fragment. PLoS ONE 7, e43746 (2012). [PubMed: 22916301]
59. Borowska MT, Dominik PK, Anghel SA, Kossiakoff AA & Keenan RJ A YidC-like protein in the archaeal plasma membrane. Structure 23, 1715–1724 (2015). [PubMed: 26256539]
60. Bailey LJ et al. Locking the elbow: improved antibody fab fragments as chaperones for structure determination. J. Mol. Biol 430, 337–347 (2018). [PubMed: 29273204]
61. Ritchie TK et al. Chapter 11 — reconstitution of membrane proteins in phospholipid bilayer nanodiscs. Methods Enzymol. 464, 211–231 (2009). [PubMed: 19903557]
62. Doublie S. Preparation of selenomethionyl proteins for phase determination. Method Enzymol. 276, 523–530 (1997).
63. Ujwal R. & Bowie JU Crystallizing membrane proteins using lipidic bicelles. Methods 55, 337–341 (2011). [PubMed: 21982781]
64. Battye TG, Kontogiannis L, Johnson O, Powell HR & Leslie AG iMOSFLM: a new graphical interface for diffraction-image processing with MOSFLM. Acta Crystallogr D Biol. Crystallogr 67, 271–281 (2011). [PubMed: 21460445]
65. Evans PR An introduction to data reduction: space-group determination, scaling and intensity statistics. Acta Crystallogr D Biol. Crystallogr 67, 282–292 (2011). [PubMed: 21460446]
66. Sheldrick GM A short history of SHELX. Acta Crystallogr. A 64, 112–122 (2008). [PubMed: 18156677]

67. Emsley P. & Cowtan K. Coot: model-building tools for molecular graphics. Acta Crystallogr D Biol. Crystallogr 60, 2126–2132 (2004). [PubMed: 15572765]
68. Murshudov GN et al. REFMAC5 for the refinement of macromolecular crystal structures. Acta Crystallogr D Biol. Crystallogr 67, 355–367 (2011). [PubMed: 21460454]
69. Kabsch W. XDS. Acta Crystallogr. D. Biol. Crystallogr 66, 125–132 (2010). [PubMed: 20124692]
70. Evans PR & Murshudov GN How good are my data and what is the resolution? Acta Crystallogr D Biol. Crystallogr 69, 1204–1214 (2013). [PubMed: 23793146]
71. Nocula-Lugowska M, Lugowski M, Salgia R. & Kossiakoff AA Engineering synthetic antibody inhibitors specific for LD2 or LD4 motifs of paxillin. J. Mol. Biol 427, 2532–2547 (2015). [PubMed: 26087144]
72. Adams PD et al. PHENIX: a comprehensive Python-based system for macromolecular structure solution. Acta Crystallogr D Biol. Crystallogr 66, 213–221 (2010). [PubMed: 20124702]
73. Skubak P. & Pannu NS Automatic protein structure solution from weak X-ray data. Nat. Commun 4, 2777 (2013). [PubMed: 24231803]
74. Brunger AT et al. Crystallography & NMR system: a new software suite for macromolecular structure determination. Acta Crystallogr. D. Biol. Crystallogr 54, 905–921 (1998). [PubMed: 9757107]
75. Brunger AT Version 1.2 of the crystallography and NMR system. Nat. Protoc 2, 2728–2733 (2007). [PubMed: 18007608]
76. Williams CJ et al. MolProbity: more and better reference data for improved all-atom structure validation. Protein Sci. 27, 293–315 (2018). [PubMed: 29067766]
77. Jo S, Kim T. & Im W. Automated builder and database of protein/membrane complexes for molecular dynamics simulations. PLoS ONE 2, e880 (2007). [PubMed: 17849009]
78. Case DA et al. AMBER 2016. 10.13140/RG.2.2.27958.70729 (2016).
79. Maier JA et al. ff14SB: improving the accuracy of protein side chain and backbone parameters from ff99SB. J. Chem. Theory Comput 11, 3696–3713 (2015). [PubMed: 26574453]
80. Dickson CJ et al. Lipid14: the amber lipid force field. J. Chem. Theory Comput 10, 865–879 (2014). [PubMed: 24803855]
81. Jorgensen WL, Chandrasekhar J, Madura JD, Impey RW & Klein ML Comparison of simple potential functions for simulating liquid water. J. Chem. Phys 79, 926–935 (1983).
82. Salomon-Ferrer R, Gotz AW, Poole D, Le Grand S. & Walker RC Routine microsecond molecular dynamics simulations with AMBER on GPUs. 2. Explicit solvent particle mesh ewald. J. Chem. Theory Comput 9, 3878–3888 (2013). [PubMed: 26592383]
83. Aqvist J, Wennerstrom P, Nervall M, Bjelic S. & Brandsdal BO Molecular dynamics simulations of water and biomolecules with a Monte Carlo constant pressure algorithm. Chem. Phys. Lett 384, 288–294 (2004).
84. Miyamoto S. & Kollman PA Settle — an analytical version of the shake and rattle algorithm for rigid water models. J. Comput. Chem 13, 952–962 (1992).
85. Gomez YK et al. Taking the Monte-Carlo gamble: how not to buckle under the pressure! J. Comput. Chem 10.1002/jcc.26798 (2021).
86. Roe DR & Cheatham TE PTRAJ and CPPTRAJ: software for processing and analysis of molecular dynamics trajectory data. J. Chem. Theory Comput 9, 3084–3095 (2013). [PubMed: 26583988]

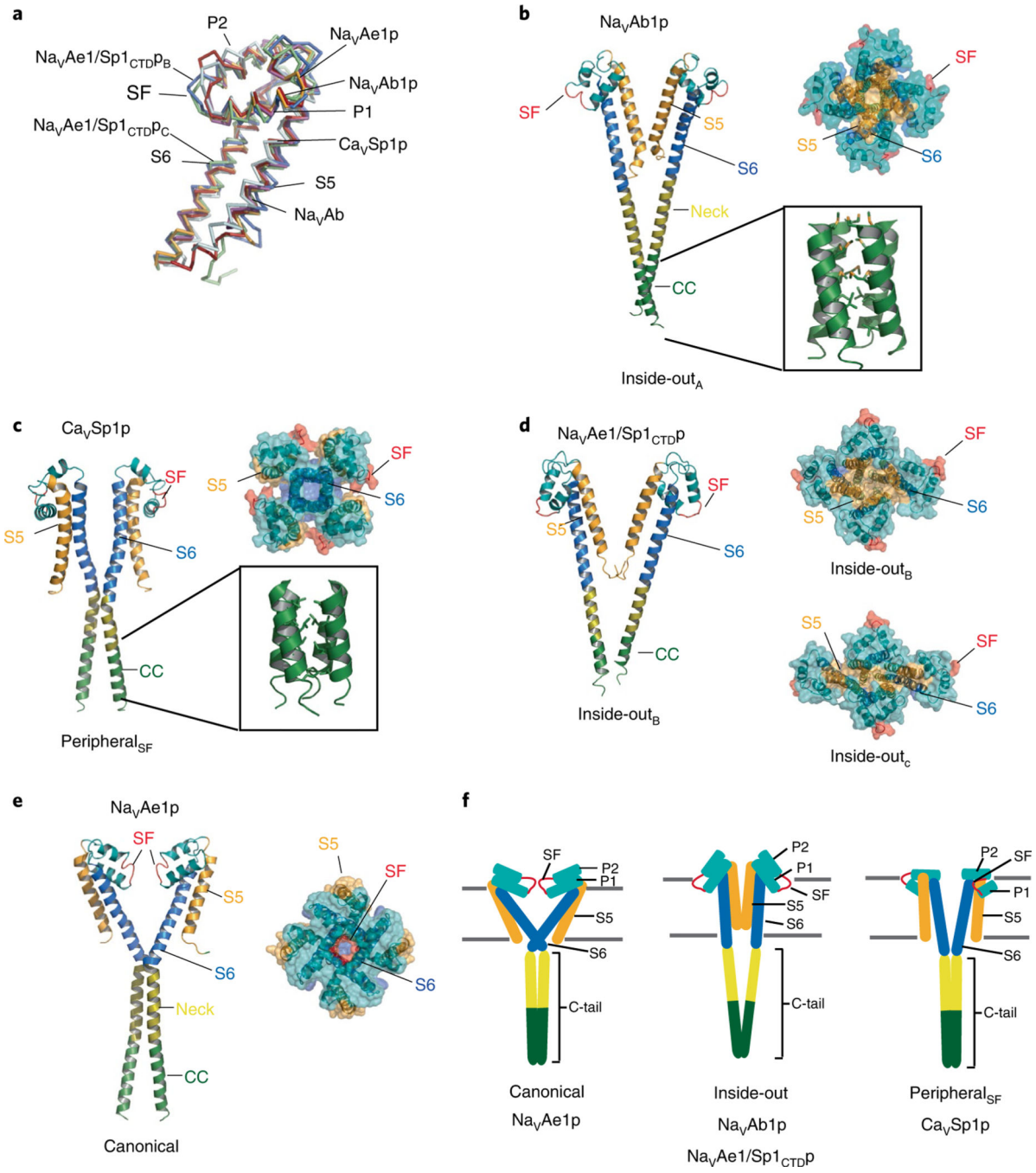

Fig. 1 |. Structures of BacNa$_V$ PDs.

a, Superposition of the PD subunits from Na$_V$Ae1p (bright orange) (PDB: 5HK7)[18], Na$_V$Ab (3RVZ) (magenta)[50], Na$_V$Ab1p (firebrick), Ca$_V$Sp1 (pale cyan), Na$_V$Ae1/Sp1$_{CTD}$p$_B$ (pale green), and Na$_V$Ae1/Sp1$_{CTD}$p$_C$ (marine blue). **b**, Na$_V$Ab1p structure, inside-out$_A$ form (left), cartoon showing two of four subunits. Upper right, extracellular view. Inset, coiled-coil. **c**, Ca$_V$Sp1p structure, peripheral$_{SF}$ form (left), cartoon showing two of four subunits. Upper right, extracellular view. Inset, coiled-coil. **d**, Na$_V$Ae1/Sp1$_{CTD}$p structure, inside-out$_B$ form (left), cartoon showing two of four subunits. Upper right and lower left, extracellular

view of inside-out$_B$ and inside-out$_C$ forms, respectively. **e**, Na_VAe1p structure, canonical form (PDB: 5HK7)[18] (left), cartoon showing two of four subunits. Right, extracellular view. **f**, Cartoon schematics of the canonical, inside-out, and peripheral$_{SF}$ quaternary structures. In **b**–**f**, channel elements are as follows, S5 (bright orange), SF (red), P1 and P2 helices (teal), S6 (marine), neck (olive), coiled-coil (forest).

Structure comparison		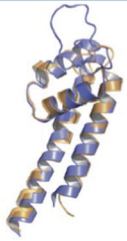		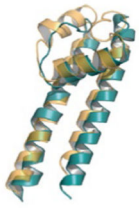	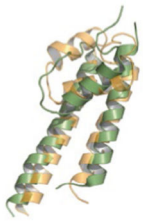
Protein (PDB)	NALCN (chain A) (7CU3)	$Ca_V1.1$ (5GJV)	TRPV1 (chain E) (5IRZ)	TRKA (chain D) (4GX1)	GluR (chain A) (5VOU)
Z-score	13.8	12.0	9.8	9.8	8.1
RMSD (Å)	1.5	1.4	2.2	2.3	2.9
ID%	26	30	11	15	8
Structure comparison	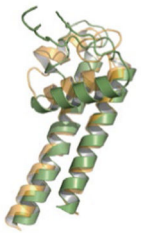		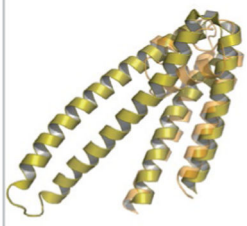	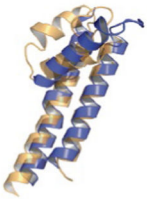	
Protein (PDB)	IP3R (6UQK)	Cellulose synthase (5JNP)	SHROOM2 (5F4Y)	TRPM2 (6PUU)	PSII chain Z (6YP7)
Z-score	7.4	6.0	6.0	5.9	5.9
RMSD (Å)	2.5	2.7	3.1	2.9	2.4
ID%	20	3	6	17	14

Fig. 2 |. Exemplar structural homologs of the VGIC-PD fold, identified using DALI[30,31].
DALI search *Z*-score, $RMSD_{C\alpha}$ (Å), and percentage identity (ID%) are shown. DALI output results are available as source data.

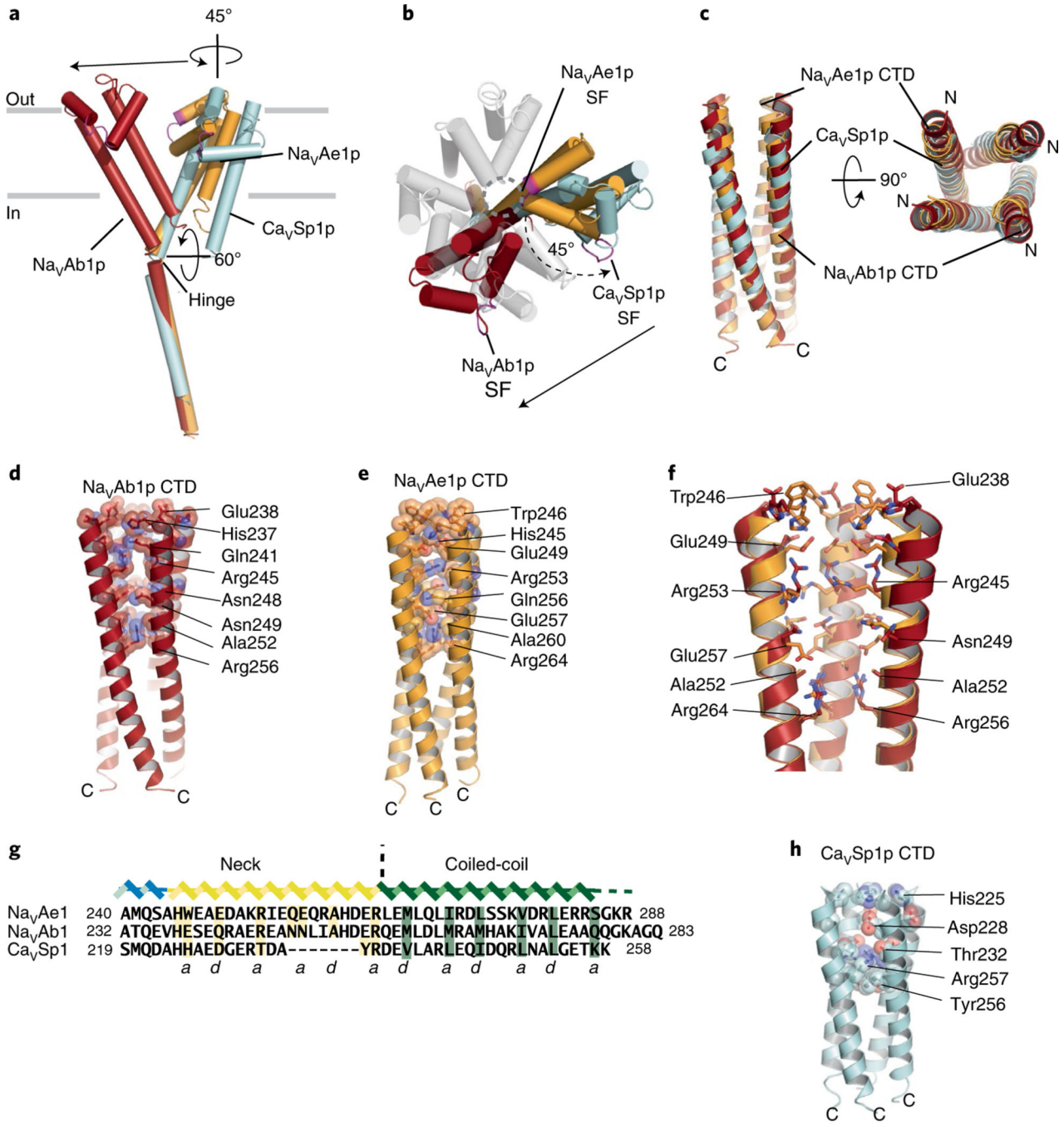

Fig. 3 |. BacNa$_V$ PD structural relationships and CTD comparisons.

a, Superpositon showing the rigid body movements that connect canonical Na$_V$Ae1p (orange), peripheral$_{SF}$ Ca$_V$Sp1p (cyan), and inside-out$_A$ Na$_V$Ab1p (firebrick) conformations. C-tails of each monomer are superposed. The selectivity filter of each monomer is magenta. Rotations indicate the Na$_V$Ae1p–Ca$_V$Sp1p and Ca$_V$Sp1p–Na$_V$Ab1p relationships. Arrows show the Ca$_V$Sp1p–Na$_V$Ab1p relationship. The hinge is indicated. **b**, extracellular view of **a**. The location of the central ion-conducting pore is indicated by the open circle. The dashed line indicates the Na$_V$Ae1p–Na$_V$Sp1p relationship. The arrow

shows the Na_VSp1p–Na_VAb1p relationship**. c**, Superposition of the CTDs of Na_VAe1p (orange), Ca_VSp1p (cyan), and Na_VAb1p (firebrick). **d**,**e**, CTDs of Na_VAb1p (**d**) and Na_VAe1p (orange) (**e**) showing the neck region hydrophilic cores as space filling. **f**, Detailed view of the superposition of the Na_VAb1p (firebrick) and Na_VAe1p (orange) neck region hydrophilic cores. **g**, Sequence alignment of the Na_VAe1p, Na_VAb1p, and Ca_VSp1p CTDs. Heptad repeat a and d positions are indicated. **h**, Ca_VSp1p CTD, showing the neck region hydrophilic core in space filling.

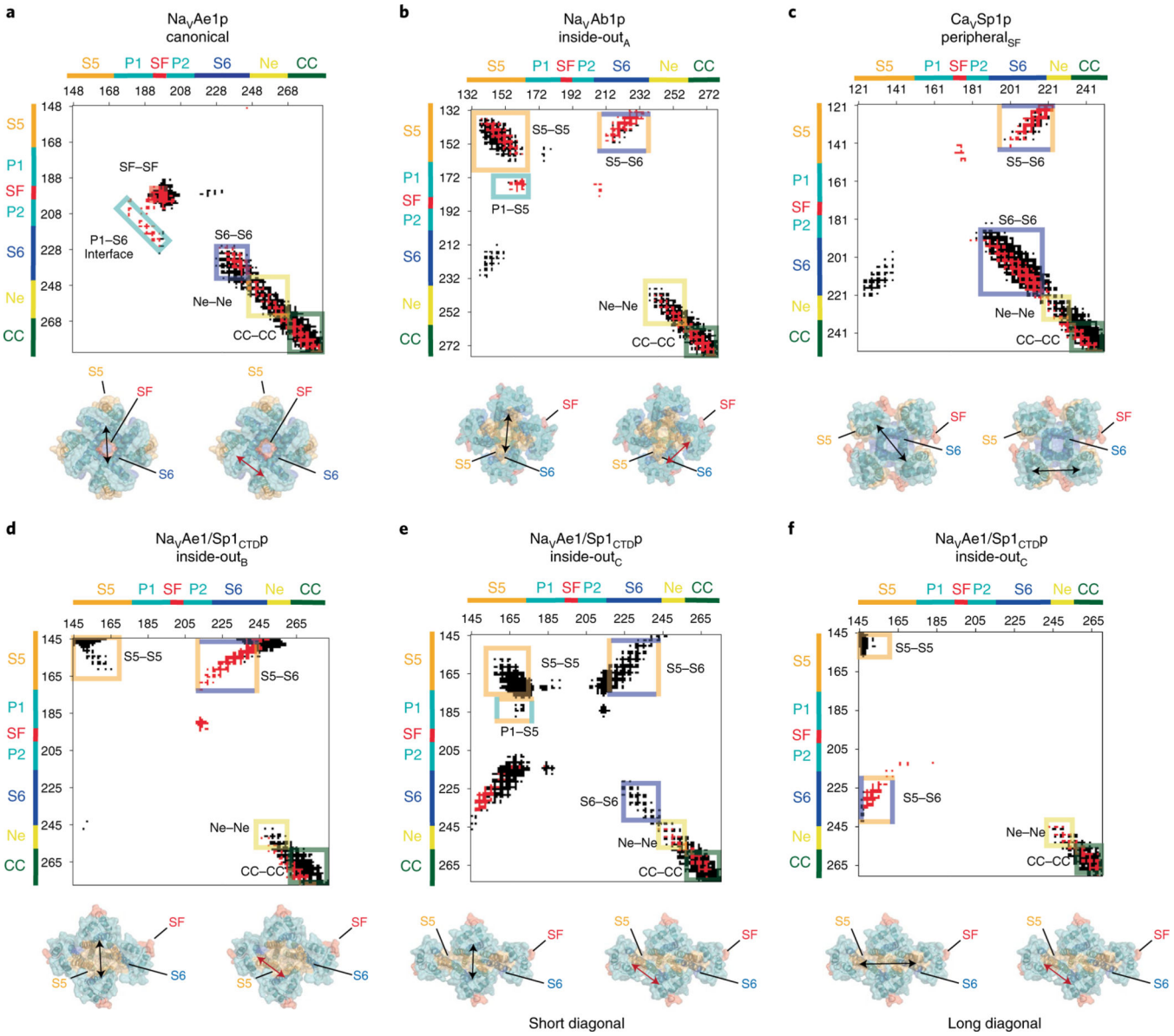

Fig. 4 |. BacNa$_V$ PD contact maps.

a–**f**, C_α–C_α distances for diagonal subunits (black) at 20 Å and neighboring subunits (red) at 12 Å for Na$_V$Ae1p, canonical conformation (**a**), Na$_V$Ab1p, inside-out$_A$ conformation (**b**), Ca$_V$Sp1p, peripheral$_{SF}$ conformation (**c**), Na$_V$Ae1/Sp1$_{CTD}$p, inside-out$_B$ conformation (**d**), Na$_V$Ae1/Sp1$_{CTD}$p, inside-out$_C$ conformation for the subunits related by the short diagonal (**e**), and Na$_V$Ae1/Sp1$_{CTD}$p, inside-out$_C$ conformation for the subunits related by the long diagonal (**f**). Channel structural elements are indicated. extracellular views of the PDs are shown underneath each plot. Arrows indicate the diagonal (black) and neighbor (red) distance relations of the contact plots.

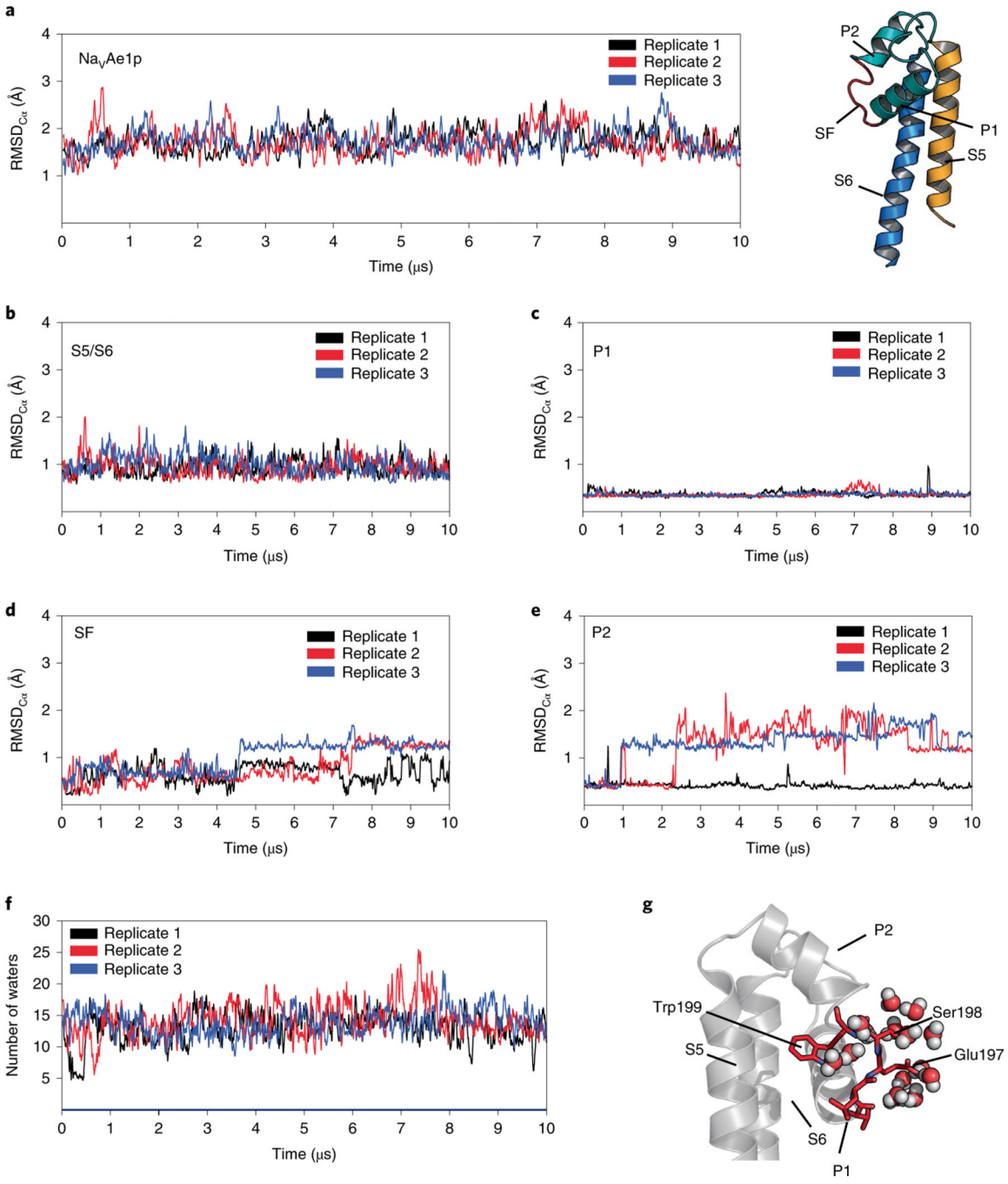

Fig. 5 |. BacNa$_V$ PD monomer is stable in a bilayer.

Na$_V$Ae1p replicate C_α root-mean-square deviation (RMSD$_{C\alpha}$) from the starting crystal structure (PDB: 5HK7)[18] as a function of time: **a**, Complete Na$_V$Ae1p monomer backbone; **b**, S5 and S6 antiparallel transmembrane helices; **c**, P1 helix; **d**, SF; and **e**, P2 helix. **f**, Plot showing number of waters within 3.0 Å of the SF (residues Thr195–Trp199) as a function of time. Replicates 1, 2, and 3, in **a**–**f** are black, red, and blue, respectively. **g**, exemplar snapshot of the hydrated selectivity filter from **f**. SF residues 195–199 are shown in red.

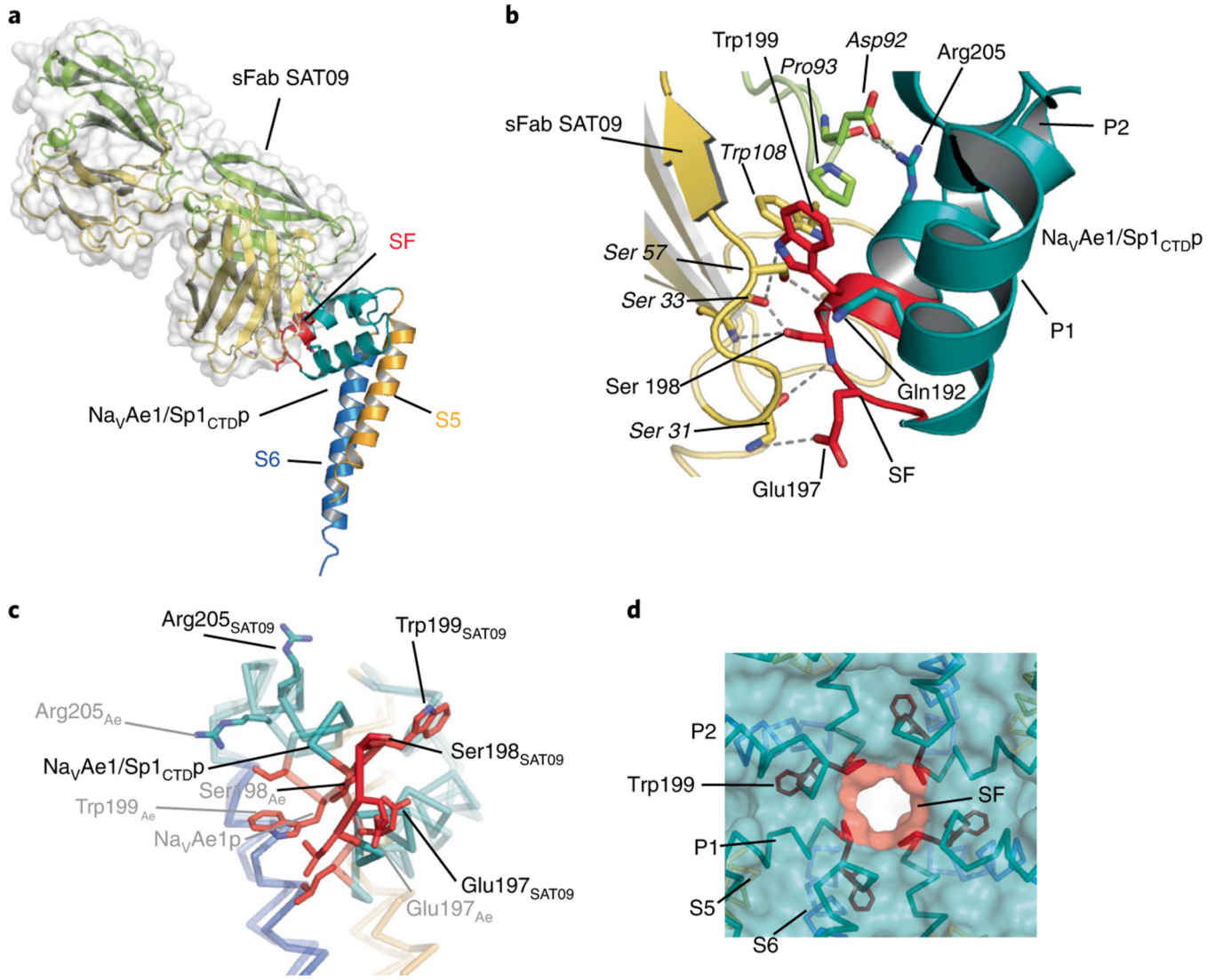

Fig. 6 |. sFab SAT09 recognizes the BacNa$_V$ SF.

a, Crystal structure of the sFab SAT09–Na$_V$Ae1/Sp1$_{CTD}$p complex. sFab SAT09 is shown with a semitransparent surface, light (lemon) and heavy (yellow orange) chains shown as cartoons. Na$_V$Ae1/Sp1$_{CTD}$p channel elements are colored as follows: S5 (bright orange), SF (red), P1 and P2 helices (teal), and S6 (marine). **b**, Details of the sFab SAT09–Na$_V$Ae1/Sp1$_{CTD}$p interface. Colors are as in **a**. **c**, Superposition of Na$_V$Ae1/Sp1$_{CTD}$p from the sFab SAT09–Na$_V$Ae1/Sp1$_{CTD}$p complex and Na$_V$Ae1p from the canonical structure (PDB: 5HK7)[18]. **d**, Quaternary context of sFab SAT09 binding epitope in the Na$_V$Ae1p canonical structure (PDB: 5HK7)[18].

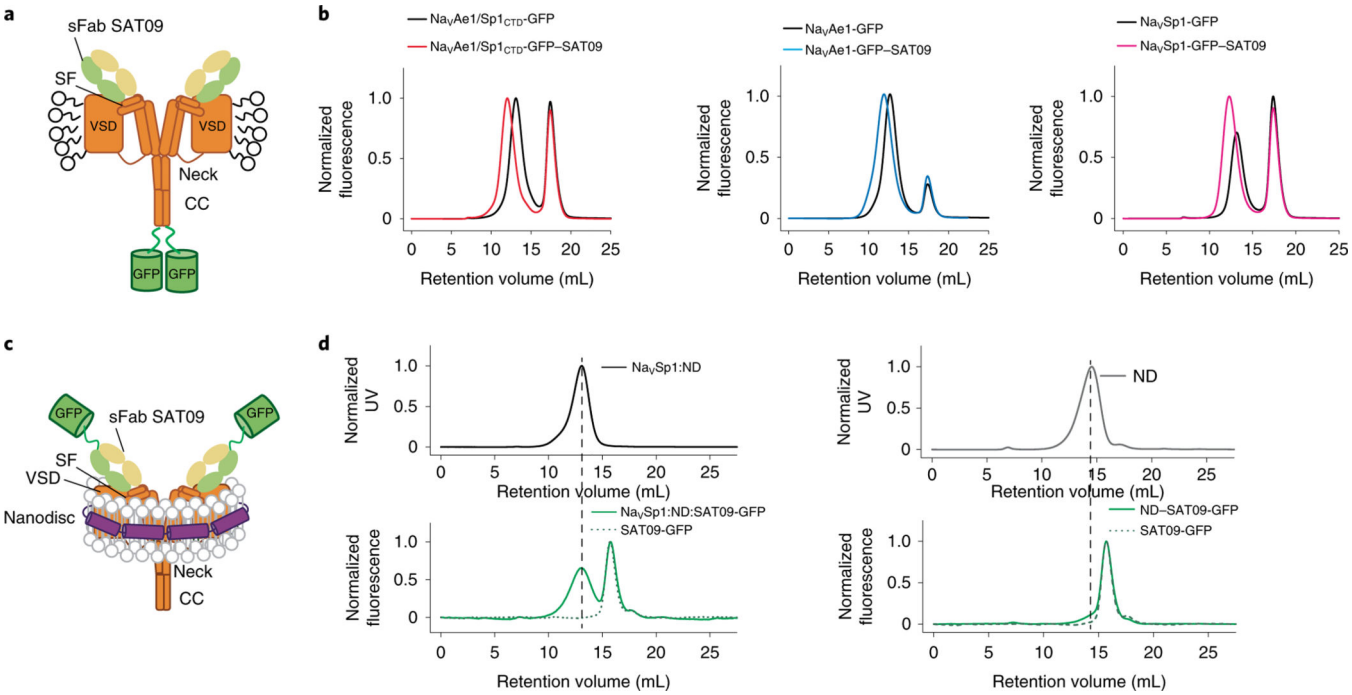

Fig. 7 |. Evidence for non-canonical PD quaternary structure in full-length BacNa$_V$s.

a, Cartoon showing the interaction of sFab SAT09 with an inside-out PD conformation in the context of a full-length BacNav in a detergent micelle. **b**, Superose 6 FSEC profiles for GFP-tagged full-length channels Na$_V$Ae1/Sp1, Na$_V$Ae1, and Na$_V$Sp1 alone and with 10 μM sFab SAT09. **c**, Cartoon showing interaction of sFab SAT09 with an inside-out PD conformation in the context of a full-length BacNav in a lipid nanodisc. **d**, Superose 6 profiles monitored by UV absorbance at 280 nm for Na$_V$Sp1–nanodiscs (ND) and ND alone (top) and FSEC for 10 μM sFab SAT09 alone (green dashed line) and with Na$_V$Sp1–ND or ND alone (bottom).

Table 1 |

Data collection and refinement statistics

	Na_VAb1p detergent (DM) (PDB: 7PGG)	**Na_VAb1p (bicelles) (PDB: 7PGi)**	**Ca_VSp1p (bicelles) (PDB: 7PGF)**	**$Na_VAe1/Sp1_{CTD}p$ (DDM) (PDB: 7PGH)**	**$Na_VAe1/Sp1_{CTD}p$–SAT09 complex (PDB: 7PGB)**	**$Na_VAe1/Sp1_{CTD}p$–ANT05 complex (PDB: 7PG8)**
Data collection						
Space group	$P4_32_12$	$I2_12_12_1$	$P6_122$	$P2_12_12_1$	$P4_3$	$P4_3$
Cell dimensions						
a, *b*, *c* (Å)	157.471, 157.471, 106.394	178.179, 191.80, 192.32	133.682, 133.682, 130.744	123.465, 134.696, 155.545	200.865, 200.865, 327.727	127.175, 127.175, 445.206
α, β, γ (°)	90, 90, 90	90, 90, 90	90, 90, 90	90, 90, 90	90, 90, 90	90, 90, 90
Resolution (Å)	111.35 – 2.85 (2.95 – 2.85)	135.81 – 3.64 (3.77 – 3.64)	115.77 – 3.5 (3.62 – 3.5)	101.82 – 4.2 (4.34 – 4.19)	200.86 – 3.6 (3.73 – 3.6)	14.99 – 4.46 (4.62 – 4.46)
R_{merge}	0.169 (>1)	0.157 (>1)	0.156 (>1)	0.065 (>1)	0.166 (>1)	0.031 (>1)
$I / \sigma I$	15.4 (1.0)	5.2 (0.9)	10.2 (0.6)	11.6 (1.1)	9.3 (0.5)	12.8 (0.7)
$CC_{1/2}$	0.999 (0.473)	0.995 (0.172)	0.995 (0.126)	0.999 (0.404)	0.998 (0.130)	0.997 (0.442)
Completeness (%)	98.99 (99.87)	98.41 (98.88)	97.17 (100.00)	96.53 (90.59)	98.47 (99.34)	98.31 (88.69)
Redundancy	16.2 (16.6)	4.2 (3.8)	11.5 (11.9)	12.9 (12.7)	7.0 (6.8)	2.0 (1.9)
Refinement						
Resolution (Å)	14.96 – 2.85	19.98 – 3.64	14.93 – 3.5	14.99 – 4.2	15 – 3.6	14.99 – 4.46
Unique reflections	31,433 (3,087)	36,662 (3,616)	8,915 (879)	18,983 (1,766)	147,489 (14,754)	42,377 (3,816)
R_{work} / R_{free}	26.6/28.0	28.7/30.4	26.5/28.9	32.8/34.30	20.8/23.4	30.3/35.2
No. atoms						
Protein	2,363	9,291	2,029	8,413	42,648	22,623
Ligand/ion	21	1	0	415	1,197	0
Water	0	0	0	0	9	0
B-factors						
Protein	98.37	130.91	153.64	319.61	190.45	251.22
Ligand/ion	152.61	104.68	N/A	277.06	186.93	N/A
Water	N/A	N/A	N/A	N/A	85.99	N/A
R.m.s. deviations						
Bond lengths (Å)	0.008	0.014	0.010	0.006	0.004	0.008

	Na_VAb1p detergent (DM) (PDB: 7PGG)	**Na_VAb1p (bicelles) (PDB: 7PGi)**	**Ca_VSp1p (bicelles) (PDB: 7PGF)**	**Na_VAe1/$Sp1_{CTD}$p (DDM) (PDB: 7PGH)**	**Na_VAe1/$Sp1_{CTD}$p–SAT09 complex (PDB: 7PGB)**	**Na_VAe1/$Sp1_{CTD}$p–ANT05 complex (PDB: 7PG8)**
Bond angles (°)	2.09	1.90	1.45	1.20	1.08	1.56

Each data set is data collected from a single crystal.

*Values in parentheses are for highest resolution shell.

Table 2 |

Data collection, phasing and refinement statistics

		$Na_VAe1_{Sp1CTD}p$ (DDM)			Na_VAb1p (DM)			Ca_VSp1p bicelles
Data collection								
Space group		$P2_12_12_1$			$P4_12_12$			$P6_122$
Cell dimensions								
a, b, c (Å)		125.43,135.80,156.13			157.6260,157.6260,106.5250			133.0465,133.0465,128.1215
α, β, γ (°)		90, 90, 90			90, 90, 90			90, 90, 90
	Peak	Inflection	Remote	Peak	Inflection	Remote	Peak	Remote
Wavelength	0.97698	0.97953	0.95368	0.97960	0.97940	0.96110	0.979764	0.957038
Resolution (Å)	48.89 – 4.51 (5.04 – 4.51)	48.77 – 4.51 (5.04 – 4.51)	48.85 – 4.51 (5.04– 4.51)	39.41 – 3.28 (3.46 – 3.28)	39.31 – 3.20 (3.37 – 3.20)	39.34 – 3.20 (3.37 – 3.2)	34.31 – 3.94 (4.40 – 3.94)	34.31 – 3.85 (4.30 – 3.85)
R_{merge}	0.044 (>1)	0.041 (>1)	0.043 (>1)	0.260 (>1)	0.182 (>1)	0.239 (>1)	0.349 (>1)	0.401 (>1)
$I/\sigma I$	10.8 (0.6)	11.6 (1.0)	11.4 (0.8)	14.2 (1.0)	19.5 (2.2)	15.7 (0.8)	16.6 (1.1)	15.2 (0.9)
$CC_{1/2}$	0.999 (0.286)	1.0 (0.439)	1.0 (0.370)	N/A	N/A	N/A	1.00 (0.282)	1.00 (0.228)
Completeness (%)	99.40 (98.30)	99.60 (98.80)	99.20 (97.70)	98.7 (92.0)	99.9 (100.0)	99.8 (99.6)	98.3 (94.7)	98.4 (95.1)
Redundancy	6.6 (6.7)	6.6 (6.8)	6.6 (6.7)	33.5 (32.2)	34.1 (35.8)	33.4 (31.7)	64.6 (33.7)	64.6 (33.6)
Unique reflections	16,246 (4,499)	16,137 (4,463)	16,169 (4,454)	20,803 (2,766)	22,495 (3,216)	22,586 (3,215)	6,214 (1,630)	6,659 (1,760)

each data set was data collected from a single crystal.

*Values in parentheses are for highest resolution shell.